

## Minimal model of $\beta$ -cell mitochondrial $\text{Ca}^{2+}$ handling

GERHARD MAGNUS<sup>1</sup> AND JOEL KEIZER<sup>1,2</sup>

<sup>1</sup>*Institute of Theoretical Dynamics and* <sup>2</sup>*Section on Neurobiology, Physiology and Behavior, University of California, Davis, California 95616*

**Magnus, Gerhard, and Joel Keizer.** Minimal model of  $\beta$ -cell mitochondrial  $\text{Ca}^{2+}$  handling. *Am. J. Physiol.* 273 (*Cell Physiol.* 42): C717–C733, 1997. — We develop a simplified, but useful, mathematical model to describe  $\text{Ca}^{2+}$  handling by mitochondria in the pancreatic  $\beta$ -cell. The model includes the following six transport mechanisms in the inner mitochondrial membrane: proton pumping via respiration and proton uptake by way of the  $\text{F}_1\text{F}_0$ -ATPase (adapted from D. Pietrobon and S. Caplan. *Biochemistry* 24: 5764–5778, 1985), a proton leak, adenine nucleotide exchange, the  $\text{Ca}^{2+}$  uniporter, and  $\text{Na}^+/\text{Ca}^{2+}$  exchange. Each mechanism is developed separately into a kinetic model for the rate of transport, with parameters taken from experiments on isolated mitochondrial preparations. These mechanisms are combined in a modular fashion first to describe state 4 (nonphosphorylating) and state 3 (phosphorylating) mitochondria with mitochondrial NADH and  $\text{Ca}^{2+}$  concentrations as fixed parameters and then to describe  $\text{Ca}^{2+}$  handling with variable mitochondrial  $\text{Ca}^{2+}$  concentration. Simulations are compared to experimental measurements and agree well with the threshold for  $\text{Ca}^{2+}$  uptake, measured mitochondrial  $\text{Ca}^{2+}$  levels, and the influence of  $\text{Ca}^{2+}$  on oxygen uptake. In the absence of  $\text{Ca}^{2+}$  activation of mitochondrial dehydrogenases, the simulations predict a significant reduction in the rate of production of ATP that involves a “short circuit” via  $\text{Ca}^{2+}$  uptake through the uniporter. This effect suggests a potential role for mitochondrial  $\text{Ca}^{2+}$  handling in determining the ATP:ADP ratio in the pancreatic  $\beta$ -cell.

pancreatic  $\beta$ -cell; oxidative phosphorylation; kinetic model; calcium uniporter; adenine nucleotide translocator

SECRETION OF INSULIN from pancreatic  $\beta$ -cells is stimulated by D-glucose and occurs via exocytosis of insulin-containing granules. The detailed mechanisms that control this process are complicated by the fact that D-glucose must be metabolized in order to stimulate secretion. Although the proximal steps of D-glucose uptake via GLUT transporters and phosphorylation by glucokinase are well characterized (46, 64), how the subsequent steps in glycolysis and mitochondrial oxidation function is not yet understood. There is general agreement, however, that glycolysis and oxidative phosphorylation lead to the production of ATP, which plays a major role in insulin secretion by inhibiting ATP-sensitive  $\text{K}^+$  ( $\text{K}_{\text{ATP}}$ ) channels in the  $\beta$ -cell. It is generally accepted that this inhibition is responsible for depolarizing the plasma membrane, which leads to  $\text{Ca}^{2+}$  influx from the external medium via voltage-dependent  $\text{Ca}^{2+}$  channels. As in other secretory cells,

increases in the concentration of intracellular  $\text{Ca}^{2+}$  ( $[\text{Ca}^{2+}]_i$ ) have been correlated with secretion (1).

The mitochondria, which are the site of oxidative phosphorylation, are another important link between glucose metabolism and  $\text{Ca}^{2+}$  handling. The role of mitochondrial  $\text{Ca}^{2+}$  handling in the regulation of metabolic processes has been emphasized frequently by Gunter and colleagues (17), and it is now more widely appreciated that mitochondria are an important component of  $\text{Ca}^{2+}$  control in certain cell types (20, 21).  $\text{Ca}^{2+}$  uptake into mitochondria appears to regulate production of ATP in two opposing manners, i.e., stimulating it via mitochondrial dehydrogenases (45) and inhibiting it by short-circuiting the  $\text{F}_1\text{F}_0$ -ATPase (28). Thus under certain circumstances an influx of  $\text{Ca}^{2+}$  into the  $\beta$ -cell might stimulate or inhibit ATP production.

Here we present a detailed model of the negative influence of  $\text{Ca}^{2+}$  uptake on ATP production, neglecting  $\text{Ca}^{2+}$  activation of the dehydrogenases. Our purpose here is to develop a “minimal model” of the most important transport processes residing in the inner mitochondrial membrane, as follows: 1) respiration-driven redox proton pumps, 2) the  $\text{F}_1\text{F}_0$ -ATPases, 3) the proton leak, 4) adenine nucleotide transporters, 5)  $\text{Ca}^{2+}$  uniporters, and 6)  $\text{Na}^+/\text{Ca}^{2+}$  exchangers (Fig. 1). We refer to the model as “minimal,” since we do not attempt to include all aspects of the interaction of mitochondrial  $\text{Ca}^{2+}$  handling with oxidative phosphorylation. For example, the stimulation of matrix dehydrogenases by  $\text{Ca}^{2+}$  has not been considered here. Indeed, by invoking quasi-steady-state approximations for several mechanisms, the final model is relatively simple, involving only three dynamic variables. As we will demonstrate, the minimal model does a good job of reproducing a variety of experimental measurements on isolated mitochondria.

Our philosophy in developing this model has been modular, i.e., we examine each component mechanism in the model separately, fine-tuning kinetic parameters to the experiment. Using the component mechanisms, we then systematically construct and test the complete model. After a brief discussion of chemiosmotic theory (MITOCHONDRIA AND OXIDATIVE PHOSPHORYLATION), we start this procedure with state 4 mitochondria, which have active redox pumps and oxidative metabolism but in which the mechanisms involved in ATP production are suppressed (STATE 4 MITOCHONDRIAL MODEL). Including adenine nucleotides as variables, while still maintaining fixed  $\text{Ca}^{2+}$  concentrations, we simulate state 3

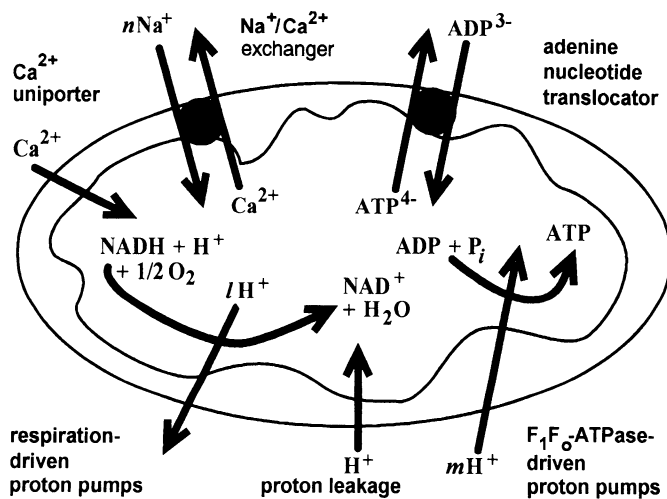


Fig. 1. Schematic representation of the ion fluxes through the mitochondrial inner membrane that have been included in the minimal model. The variable  $\text{H}^+:\text{e}^-$  and  $\text{H}^+:\text{ATP}$  ratios for proton ejection and uptake by the respiration- and  $\text{F}_1\text{F}_0$ -ATPase-driven proton pumps are given by the factors  $l$  and  $m$ , respectively. The  $n\text{Na}^+$  shown for the  $\text{Na}^+/\text{Ca}^{2+}$  exchanger indicates the uncertain stoichiometry for that carrier.

mitochondria by adding the  $\text{F}_1\text{F}_0$ -ATPase and the adenine nucleotide translocator to the state 4 model (STATE 3 MITOCHONDRIAL MODEL). Finally, the full minimal model is developed in which the  $\text{Ca}^{2+}$  uniporter and  $\text{Na}^+/\text{Ca}^{2+}$  exchanger are added to the state 3 model (CALCIUM HANDLING BY MITOCHONDRIA). At each step the results of the model are compared with experiment. The full minimal model is used to simulate steady-state  $\text{Ca}^{2+}$  handling by isolated mitochondria and responses to brief pulses of  $\text{Ca}^{2+}$  (FULL MINIMAL MODEL). This provides quantitative predictions of the influence of  $\text{Na}^+/\text{Ca}^{2+}$  exchange and relative densities of the uniporter and exchanger on the time course and threshold of  $\text{Ca}^{2+}$  uptake. Although the model was developed with specific application to the pancreatic  $\beta$ -cell in mind, it may have application to mitochondrial  $\text{Ca}^{2+}$  handling in other cell types in which  $\text{Ca}^{2+}$  uptake by mitochondria has been shown to be important (20, 21).

#### MITOCHONDRIA AND OXIDATIVE PHOSPHORYLATION

Most islet ATP is synthesized in the mitochondria by the process of oxidative phosphorylation. The general statement of chemiosmotic theory provides a theoretical framework for understanding the underlying transfers of energy, which link the chemical reactions of substrate oxidation and ADP phosphorylation through an electrochemical potential across the mitochondrial inner membrane (47). The modern version of this theory, which includes all the major transmembrane currents as well as other nonspecific sources of energy dissipation, is used here to model the synthesis of ATP in  $\beta$ -cells.

Under physiological conditions, the free energy of the electron transfer between a succession of membrane-embedded carrier proteins (complexes I through IV) drives the ejection of protons from the matrix to the cytosol by way of three energy-conserving sites. The proton-motive force (PMF,  $\Delta p$ ) generated by the proton

fluxes occurring at these sites stores the free energy derived from oxidation in the form of a voltage difference ( $\Delta\psi$ ) and a pH difference ( $\Delta\text{pH}$ , see Table 1) across the inner mitochondrial membrane. The energy stored in the membrane is then  $\Delta p = \Delta\psi - (2.303RT/F) \cdot \Delta\text{pH}$ , where  $R$  is the gas constant,  $T$  is the absolute temperature,  $F$  is Faraday's constant, and all gradients are written with the matrix as the reference. For mitochondria in situ, both terms of the PMF contribute to the maintenance of a counterflux of protons back into the matrix. The energy from the voltage and pH gradients is then used by the  $\text{F}_1$ -subunit of mitochondrial  $\text{F}_1\text{F}_0$ -ATPase to synthesize ATP (47, 63).

In addition to driving  $\text{H}^+$  reuptake, polarization of the inner membrane acts to limit mitochondrial respiration. This negative feedback, known as "respiratory control," decreases the rates of both electron transfer and oxidation for large values of  $\Delta\psi$ . The more polarized the membrane, the lower the oxygen consumption and net rate of  $\text{H}^+$  cycling between the matrix and cytosol. Conversely, transmembrane fluxes resulting in a net flow of positive charge into the matrix have a stimulatory effect on respiration and oxidative metabolism (47, 63).

Suspensions of aerobic mitochondria are said to be in respiratory state 4 when ATP production and  $\text{H}^+$  reuptake have been blocked, usually by application of the  $\text{F}_1\text{F}_0$ -ATPase inhibitor oligomycin (63). State 4 is also favored by inhibiting the adenine nucleotide translocator with atractyloside. The influx of  $\text{Ca}^{2+}$  is often minimized in state 4 by including ethylene glycol-bis( $\beta$ -aminoethyl ether)- $N,N,N',N'$ -tetraacetic acid (EGTA) in the medium or the  $\text{Ca}^{2+}$  uniporter antagonist ruthenium red. The only significant currents remaining in state 4 mitochondria at steady state are currents associated with respiration-driven  $\text{H}^+$  ejection and the dissipative leakage of cytosolic protons back into the matrix (14). This slow  $\text{H}^+$  cycling under "static head" conditions reflects the control exerted by an elevated membrane potential on respiratory chain electron flow and oxygen consumption.

In idealized state 4 mitochondria, the small net movement of mitochondrial protons across the inner membrane would be near equilibrium (51). The net transmembrane  $\text{H}^+$  influx ( $J_{\text{H}}$ ) could then be written as a sum of forces with constant coefficients. At steady state this would give

$$\Delta p = \frac{sn}{g_{\text{H}}} J_0 \quad (1)$$

where  $J_0 = J_{\text{H}}/2$  is the single-atom oxygen consumption rate,  $g_{\text{H}}$  is the conductance for inward  $\text{H}^+$  leakage (see Table 1),  $s$  is the number of active energy-conserving sites, and  $n$  the number of protons pumped out (per 2 electrons) at each site. Since near-equilibrium conditions require that the coefficients of  $J_0$  and  $\Delta p$  are constant, the inner membrane should have an ohmic  $\text{H}^+$  conductance, and  $\Delta p$  should always be proportional to  $J_0$  in state 4. However, this ideal relationship is not observed experimentally (32). Furthermore, nonlinear conductance functions for  $\text{H}^+$  leakage depend on the

Table 1. *Model parameters*

Quantity	Value	Reference
$\Delta\text{pH}$ $\text{pH}_i - \text{pH}_m$	-0.4	50, 62
$T$ Temperature	310K	
$g_H$ $\text{H}^+$ leakage conductance	$0.2 \text{ nmol} \cdot \text{min}^{-1} \cdot \text{mV}^{-1} \cdot \text{mg protein}^{-1}$	47, 69
$C_{\text{mito}}$ Inner membrane capacitance	$1.45 \times 10^{-3} \text{ nmol} \cdot \text{mV}^{-1} \cdot \text{mg protein}^{-1}$	18

$\text{pH}_i$ , intercellular pH;  $\text{pH}_m$ , mitochondrial pH.

electron acceptor present in vitro and the type of respiratory inhibitor used to vary  $\Delta p$  and  $J_o$  (51). These results imply that the stoichiometry of  $\text{H}^+$  ejection is variable and probably voltage dependent and that a further dissipation of respiratory energy in addition to that caused by  $\text{H}^+$  leakage occurs at the “energy-conserving” sites of the respiratory chain (53, 69). Thus a more realistic model for the coupling of respiration to proton pumping is required (STATE 4 MITOCHONDRIAL MODEL).

Mitochondria in respiratory state 3 are characterized by the availability of ADP and  $\text{P}_i$ . In terms of chemiosmotic theory, the inner membrane voltage is lowered by an influx of protons that drives the production of ATP by the  $\text{F}_1\text{F}_0$ -ATPase, while diminished respiratory control raises the rates of oxygen consumption, electron transfer, and substrate oxidation (47). Membrane depolarization also occurs as a result of an electrogenic exchange of matrix  $\text{ATP}^{4-}$  for external  $\text{ADP}^{3-}$  mediated by the adenine nucleotide translocator (31). Uptake of the  $\text{P}_i$  needed for oxidative phosphorylation occurs via proton/phosphate symport, without any net charge transfer, while the  $\Delta\text{pH}$  term of the PMF affects inter-compartmental equilibration of  $\text{P}_i$  and other anionic substrates (63). As in the state 4 system, we initially ignore the electrogenic transport of divalent cations, especially  $\text{Ca}^{2+}$  (STATE 3 MITOCHONDRIAL MODEL).

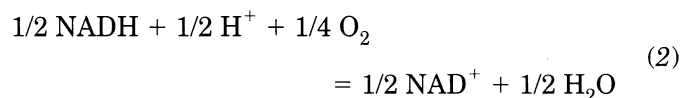
#### STATE 4 MITOCHONDRIAL MODEL

Pietrobon and colleagues (52, 53) have modeled steady-state electron transfer and the accompanying  $\text{H}^+$  efflux using a proton pump mechanism, an approach based on the diagram method of Altman and King as extended by Hill (22). In adapting this model to  $\beta$ -cell mitochondria in situ, we have treated the driving force provided by NADH oxidation as incompletely coupled to the outward flow of protons. This allows for a  $\Delta\Psi$ -dependent  $\text{H}^+/\text{e}^-$  stoichiometry and a vastly superior representation of experimental measurements.

In this simplified model, the six states of the respiratory chain proton pumps are represented by the vertices of a diagram (Fig. 2). Each pump is responsible for the  $\text{H}^+$  ejection linked to the transfer of a single electron from NADH-coenzyme Q reductase through cytochrome oxidase. States on the *left* of the diagram in Fig. 2 are associated with transformations on the mitochondrial side of the inner membrane, whereas cytosolic-oriented states are grouped on the *right*; the connecting lines correspond to the possible state transitions. Although these are all treated as first order, the

corresponding rate constants may actually be functions of extrinsic quantities affecting pump turnover (membrane potential, ligand and metabolite concentrations, etc.). Detailed balance requires that the rate constants in a cycle are not independent. The equilibrium ratios of occupancy of the states for deenergized mitochondria have been chosen to bias states oriented toward the matrix.

At steady state, the steps completing any uncrossed loop in the diagram all have the same net rate or cycle flux, which is treated as positive for the counter-clockwise direction. The positive loop following the perimeter of the diagram (*cycle a*) represents the binding to the pump of 6  $\text{H}^+$  ( $1 \rightarrow 2$ ), and their subsequent release to the cytosol ( $5 \rightarrow 6$ ). This  $\text{H}^+$  ejection is completely coupled to the driving reaction



which enables the energized pump to undergo a conformational change reorienting its  $\text{H}^+$  binding sites from the matrix to the cytosol ( $4 \rightarrow 5$ ). Rate constants for the proton unbinding steps  $2 \rightarrow 1$  and  $5 \rightarrow 6$  involve boundary potentials that are measured at each membrane surface with respect to the nearest bulk phase, and sum to a constant boundary voltage difference ( $\Delta\Psi_B$ ) = 50 mV. The corresponding conformational changes  $1 \rightarrow 6$  and  $6 \rightarrow 1$  occur within the membrane itself and are assumed to surmount a single symmetrical Eyring barrier; hence, the rate constants depend on  $\Delta\Psi - \Delta\Psi_B$  rather than on  $\Delta\Psi$ .

In *cycle a* of the original Pietrobon-Caplan model, the transfer of a single electron as part of the oxidation of  $1/2$  succinate drives a total ejection of 4  $\text{H}^+$  at *sites 2*

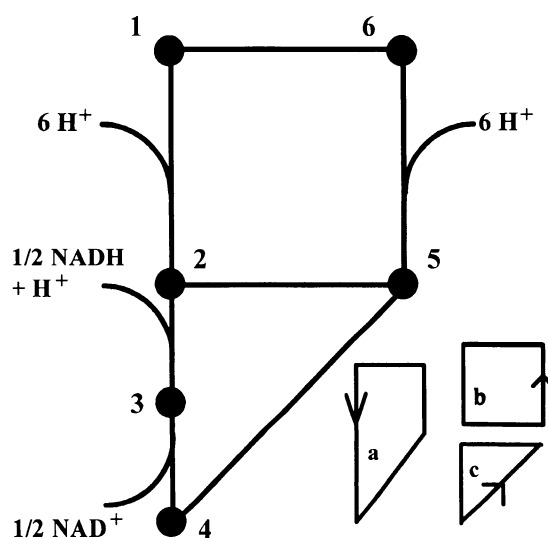


Fig. 2. Altman-King-Hill diagram for a respiration-driven proton pump. States with the pump oriented toward the matrix are on the *left*; those with the pump oriented toward the cytosol are on the *right*. A counter-clockwise cycle of the diagram's perimeter corresponds to the transfer of  $1 \text{ e}^-$  and the ejection of a maximum of 6  $\text{H}^+$ , as driven by the oxidation of  $1/2$  NADH in the mitochondrial inner membrane. Further details appear in the text. *a*, *b*, *c*: Cycles *a*, *b*, *c*.

and 3 (52, 53). This stoichiometry is ideal in that the coupling of respiratory and electrochemical energies during substrate oxidation and proton ejection is assumed to be complete. An analogous stoichiometry of  $10:2\text{e}^-:3.5\text{--}4\text{ H}^+$  per site has been proposed for respiration-driven  $\text{H}^+$  efflux by Lehninger and co-workers (8) on the basis of experiments using rat liver mitochondria. Our version of the proton pump model uses these results but replaces complex II input with that of NADH at complex I, hence linking the oxidation of  $1/2$  NADH to a net ejection of  $6\text{ H}^+$  in cycle *a* ( $1/2\text{O}:1\text{e}^-:3\text{ site}\cdot2\text{ H}^+/\text{site} = 6\text{ H}^+$ ). These changes entail some modifications of the rate constants and an adjustment to the  $\Delta\Psi$  dependence of the final rate laws (Table 2 and APPENDIX A).

The diagram's other two cycles (*b* and *c*) create a potential "short circuit" for cycle *a* determined by the magnitude of the  $5 \leftrightarrow 2$  rate constants. In "reaction slip" (cycle *c*), NADH oxidation occurs without  $\text{H}^+$  ejection ( $2 \rightarrow 3 \rightarrow 4 \rightarrow 5 \rightarrow 2$ ). "Proton slip" in cycle *b*, although less likely, corresponds to an outward  $\text{H}^+$  leakage that occurs independently of the chemical driving force. The total single-electron transfer rate at steady state consists then of a major component completely coupled to  $\text{H}^+$  ejection (cycle *a*) and another representing a dissipation of respiratory energy (cycle *c*); similarly, total  $\text{H}^+$  efflux sums the fluxes of cycles *a* and *b*.

Mitochondrial NAD ( $[\text{NADH}]_{\text{m}}$  and  $[\text{NAD}^+]_{\text{m}}$ ) is assumed to be conserved (see Ref. 63), i.e.

$$[\text{NADH}]_{\text{m}} + [\text{NAD}^+]_{\text{m}} = 8\text{ nmol/mg protein} \quad (3)$$

where  $1\text{ nmol/mg protein} \approx 1.25\text{ mM}$  in terms of mitochondrial volume (36). The concentration of matrix NAD is not constant, as would be analogous to the fixed fumarate concentration in the original model. This necessitates that the  $4 \rightarrow 3$  transition be redefined in terms of a variable  $[\text{NAD}^+]_{\text{m}}$ . In the modified model, we have also changed the pH values to mitochondrial pH ( $\text{pH}_{\text{m}} = 7.6$  and intercellular pH ( $\text{pH}_{\text{i}} = 7.2$ , which are representative of the  $\beta$ -cell. In both models, the steady-state  $\Delta\text{pH}$  is approximated as constant, with the  $\beta$ -cell value of  $-0.4$  in agreement with measurements made

Table 2. *Respiration-driven  $\text{H}^+$  pump parameters*

Quantity		Value	Reference
$K_{\text{res}}$	Equilibrium constant for Eq. 2	$1.35 \times 10^{18}$	38
$\rho_{\text{res}}$	$\text{H}^+$ pump concentration	$0.4\text{ nmol/mg protein}$	63
$r_1$	Sum of $\alpha_i$ products	$2.077 \times 10^{-18}$	40, 52
$r_2$	Sum of $\alpha_i$ products	$1.728 \times 10^{-9}$	40, 52
$r_3$	Sum of $\alpha_i$ products	$1.059 \times 10^{-26}$	40, 52
$r_a$	Sum of $\alpha_i$ products	$6.394 \times 10^{-10}/\text{s}$	40, 52
$r_b$	Sum of $\alpha_i$ products	$1.762 \times 10^{-13}/\text{s}$	40, 52
$r_{c1}$	Sum of $\alpha_i$ products	$2.656 \times 10^{-19}/\text{s}$	40, 52
$r_{c2}$	Sum of $\alpha_i$ products	$8.632 \times 10^{-27}/\text{s}$	40, 52
$\Delta\Psi_{\text{B}}$	Total phase boundary potentials	$50\text{ mV}$	52
$g$	Fitting factor for voltage	$0.85\text{ (adjusted)}$	

See Eq. 5 and APPENDIX A.

denominators containing nearly 100 terms, each a product of 5 rate constants. We have found, on the basis of algebraic manipulations and numerical substitutions for the variables, that these expressions can be approximated to within 10% accuracy by much simpler ones, which we have then used in our simulations (cf Eqs. 5 and 6, below). We have approximated numerous terms and factors in the full expressions by numerical constants. These constants,  $r$ , appearing in the simplified expressions are subscripted either by the letter of the cycle with which they are associated, or else the number when appearing in the denominator common to both  $J_{\text{res}}$  (Eq. 5) and  $J_{\text{H,res}}$  (Eq. 6). The numerical coefficients of the rate constants set by Pietrobon and Caplan (52), except for those corresponding to the diagram's slip transitions ( $2 \rightarrow 5$  and  $5 \rightarrow 2$ ), have been used to calculate all of the  $r$  values (Table 2). Also appearing in these rate expressions is the affinity ( $A_{\text{res}}$ ) of the driving reaction (Eq. 2; with equilibrium constant  $K_{\text{res}}$ )

$$A_{\text{res}} = \frac{RT}{F} \ln \left( \frac{K_{\text{res}} \sqrt{[\text{NADH}]_{\text{m}}}}{\sqrt{[\text{NAD}^+]_{\text{m}}}} \right) \quad (4)$$

Since the single oxygen atom consumption rate  $J_{\text{o}}$  is one-half that of  $J_{\text{res}}$ , a conversion to units of nmol O (per minute per milligram protein) yields

$$J_{\text{o}} = 30\rho_{\text{res}} \frac{\left[ r_a 10^{6\Delta\text{pH}} + r_{c1} \exp\left(\frac{6F\Delta\Psi_{\text{B}}}{RT}\right) \right] \exp\left(\frac{FA_{\text{res}}}{RT}\right) - r_a \exp\left(\frac{g6F\Delta\Psi}{RT}\right) + r_{c2} \exp\left(\frac{FA_{\text{res}}}{RT}\right) \exp\left(\frac{g6F\Delta\Psi}{RT}\right)}{\left[ 1 + r_1 \exp\left(\frac{FA_{\text{res}}}{RT}\right) \right] \exp\left(\frac{6F\Delta\Psi_{\text{B}}}{RT}\right) + \left[ r_2 + r_3 \exp\left(\frac{FA_{\text{res}}}{RT}\right) \right] \exp\left(\frac{g6F\Delta\Psi}{RT}\right)} \quad (5)$$

in isolated liver cells (50, 62). Rate constants for the slip transitions determining the *a* and *c* cycle fluxes have been set on the basis of simulations using the differential equation for  $\Delta\Psi$  (cf Eq. 8, below).

The steady-state rates of single-electron transfer ( $J_{\text{res}}$ ) and the corresponding  $\text{H}^+$  efflux ( $J_{\text{H,res}}$ ) derived from the diagram of Fig. 2 are large fractions with

Here  $\rho_{\text{res}} = 0.4\text{ nmol/mg protein}$  is the proton pump density estimated from respiratory chain enzyme concentrations (63). The factor  $g = 0.85$  shifts the inflection point of both  $\Delta\Psi$ -dependent curves closer to that obtained by Pietrobon and Caplan (52) in their succinate-driven system and may represent the fraction of the potential that is actually felt by the proton pumps in

the membrane. The  $\text{H}^+$  ejection rate includes a factor of 6 corresponding to the ideal  $\text{H}^+:\text{e}^-$  ratio (8)

$$J_{\text{H, res}} = 360\rho_{\text{res}} \frac{r_a 10^{6\Delta\text{pH}} \exp\left(\frac{FA_{\text{res}}}{RT}\right) - [r_a + r_b] \exp\left(\frac{g6F\Delta\Psi}{RT}\right)}{\left[1 + r_1 \exp\left(\frac{FA_{\text{res}}}{RT}\right)\right] \exp\left(\frac{6F\Delta\Psi_B}{RT}\right) + \left[r_2 + r_3 \exp\left(\frac{FA_{\text{res}}}{RT}\right)\right] \exp\left(\frac{g6F\Delta\Psi}{RT}\right)} \quad (6)$$

Following classical electrophysiology, we treat the inner mitochondrial membrane as an electric circuit with resistance and capacitance. Thus the dielectric properties are represented by a capacitance ( $C_{\text{mito}}$ ), and parallel conductances correspond to the various ion channels and electrogenic carriers. Since  $\text{Ca}^{2+}$  transport has been blocked in our state 4 model, the only currents are  $J_{\text{H, res}}$  and the ohmic  $\text{H}^+$  leakage ( $J_{\text{H, leak}}$ ), with a conductance  $g_{\text{H}} = 0.2 \text{ nmol} \cdot \text{min}^{-1} \cdot \text{mV}^{-1} \cdot \text{mg protein}^{-1}$  as measured for rat liver mitochondria (see Ref. 47), i.e.

$$J_{\text{H, leak}} = g_{\text{H}} \Delta p \quad (7)$$

Assuming a capacitance of  $C_{\text{mito}} = 1.45 \times 10^{-3} \text{ nmol} \cdot \text{mV}^{-1} \cdot \text{mg protein}^{-1}$  (18) and applying Kirchhoff's current law to Eqs. 6 and 7, we obtain a differential for the inner membrane voltage in state 4

$$C_{\text{mito}} \frac{d\Delta\Psi}{dt} = -(-J_{\text{H, res}} + J_{\text{H, leak}}) \quad (8)$$

As is conventional, inward cationic currents are taken as positive, and unsigned fluxes are assumed to be positive under physiological conditions. Note that we use the empirical units for capacitance, nanomoles per millivolt per milligram protein.

The cycling of  $\text{H}^+$  ejection to the cytosol and its  $\Delta p$ -driven return back into the matrix accounts for only about 30% of state 4 respiration (69), a fraction which corresponds to the contribution of cycle flux  $a$  to  $J_{\text{res}}$ . This result is used in conjunction with Eq. 8 and the near-maximal levels of  $[\text{NADH}]_{\text{m}}$  (Eq. 3) typical of state 4 (14, 63) to set the rate constant for the  $5 \rightarrow 2$  transition.

To obtain the steady-state value of the membrane potential for a fixed value of  $[\text{NADH}]_{\text{m}}$ , we set the right side of Eq. 8 equal to zero and solve the resulting equation

$$J_{\text{H, res}} = J_{\text{H, leak}} \quad (9)$$

for  $\Delta\Psi$  using the expressions in Eqs. 6 and 7. For our standard parameters this gives the result shown in Fig. 3A.

The simulated values of  $J_{\text{H, leak}} = 41 \text{ nmol} \cdot \text{min}^{-1} \cdot \text{mg protein}^{-1}$  and  $\Delta\Psi = 180 \text{ mV}$  are in good agreement with experimental results for static head conditions, for which the inner membrane is more polarized than in phosphorylating (state 3) mitochondria (14, 54, 69). Additional simulations predict that lowering the driving force by several orders of magnitude from the levels

corresponding to maximally reduced NAD will have little effect on  $\Delta\Psi$  (Fig. 3A). However,  $J_o$  continues to

increase as the membrane voltage rises (Fig. 3B), with the parallel contribution of reaction slip exceeding that associated with a near-constant  $\text{H}^+$  ejection rate for  $\Delta\Psi > 172 \text{ mV}$ .

### STATE 3 MITOCHONDRIAL MODEL

Here we introduce a simplifying assumption analogous to Eq. 3, namely, that the total concentrations of  $\text{ATP} + \text{ADP}$  in the cytosol and in the matrix ( $[\text{ATP}]_{\text{m}} + [\text{ADP}]_{\text{m}}$ ) separately remain constant. This requires that  $\text{ADP}^{3-}/\text{ATP}^{4-}$  exchange be the predominant mechanism for mitochondrial adenine nucleotide transport

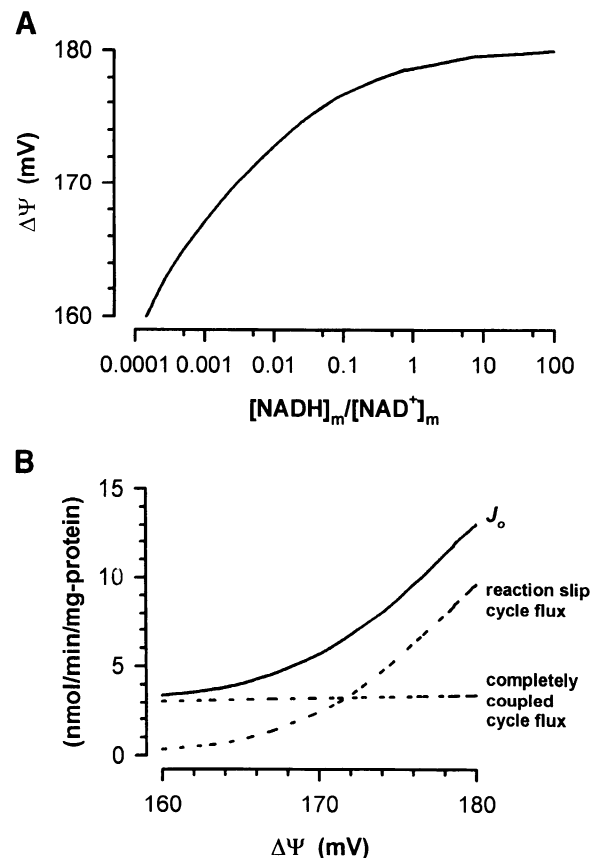


Fig. 3. Steady-state characteristics of state 4 mitochondria with blocked  $\text{Ca}^{2+}$  transport, as simulated using Eq. 8. A: the membrane voltage ( $\Delta\Psi$ ) approaches a maximum as the matrix NAD is increased to the reduced levels associated with static head. However, instead of saturating, the single-atom oxygen consumption ( $J_o$ ) continues to rise (B), due to the increasing contribution of reaction slip cycle flux to the electron transfer rate (the terms with factors  $r_{c1}$  and  $r_{c2}$  in Eq. 5.  $[\text{NADH}]_{\text{m}}/[\text{NAD}^+]_{\text{m}}$ , mitochondrial NAD ratio.

and ignores conversion reactions involving AMP. The conservation condition for the matrix is based on measurements from hepatocyte mitochondria (12, 65)

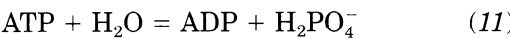
$$[\text{ATP}]_m + [\text{ADP}]_m = 12 \text{ nmol/mg protein} \quad (10)$$

which is in reasonable agreement with results obtained after the fractionation of rat islets (41). Preparations of state 3 mitochondria are able to maintain high levels of ATP production despite ongoing phosphorylation of ADP, because of the presence of such ADP-regenerating systems as D-glucose/glucokinase. We simulate these in vitro conditions by fixing the extramitochondrial ATP and ADP concentrations.

Mechanisms for the reactions that determine the homeostasis of adenine nucleotides are frequently expressed in terms of the concentrations of reactants that are unbound, ionized, or complexed with various cations. Such distributions may be approximated by coefficients representing the fractions of unbound ATP and ADP in the matrix and extramitochondrial compartments and the further proportions of these free concentrations existing in the ionized forms  $\text{ATP}^{4-}$  and  $\text{ADP}^{3-}$ . Fixed site ATP binding is assumed to be negligible throughout the  $\beta$ -cell, and setting  $[\text{ADP}]_{m,\text{free}} = 0.8[\text{ADP}]_m$  is consistent with experiments using mitochondrial fractions of excited islets (41). Although about 70% of cytosolic ADP concentration ( $[\text{ADP}]_i$ ) is bound to fixed sites (16),  $[\text{ADP}]_{i,\text{free}} = [\text{ADP}]_i$  for preparations of isolated mitochondria simulated here.

The proportions of the unbound species that are completely ionized are determined primarily by the level of  $\text{Mg}^{2+}$ . Characteristic fractions have been calculated using measurements from hepatocytes or solutions that duplicate cytoplasmic cation concentrations (12). Assuming these proportionalities are similar for the cytosol and matrix, we propose the approximate distributions are  $[\text{ATP}^{4-}] = 0.05[\text{ATP}]$  and  $[\text{ADP}^{3-}] = 0.45[\text{ADP}]_{\text{free}}$ .

In analogy to their description of respiration-driven  $\text{H}^+$  efflux, Pietrobon and Caplan (52) have modeled the mitochondrial  $\text{F}_1\text{F}_0$ -ATPase as the bidirectional, six-state proton pump illustrated in Fig. 4. This pump is driven by the reaction



If mitochondrial electron transfer is inhibited, ATP hydrolysis by the  $\text{F}_1$ -ATPase is coupled to  $\text{H}^+$  ejection through the pore-like  $\text{F}_0$  sector (63). This corresponds to the positive, counterclockwise direction of the undissipated cycle *a* (Fig. 4), with added contributions from the proton and reaction slip cycles *b* and *c* that depend on the magnitudes of the  $2 \leftrightarrow 5$  rate constants. In vivo, however, the system operates in the reverse direction, with the force of the proton electrochemical gradient now providing the energy essential for some step in the synthesis of ATP. This description is consistent with a mechanism in which the  $\text{H}^+$  backflow coupled to the phosphorylation reaction ( $5 \rightarrow 4$ ) induces long-range conformational changes in the  $\text{F}_1$  catalytic subunits without actually entering them. The ideal stoichiom-

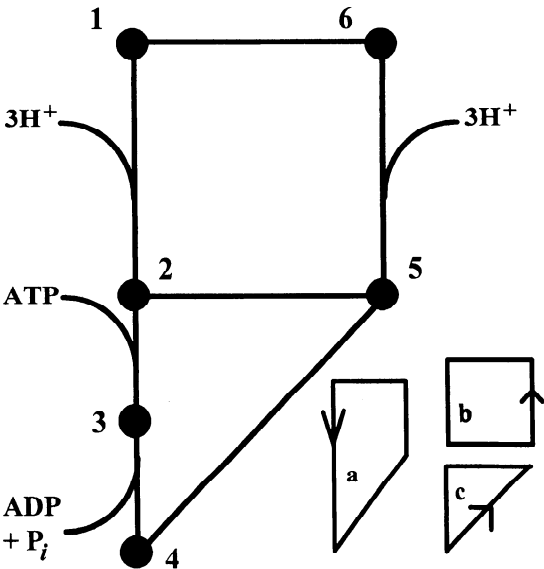


Fig. 4. Altman-King-Hill diagram for an ATPase-driven proton pump. States with the pump oriented toward the matrix are on the left; those with the pump oriented toward the cytosol are on the right. A counter-clockwise cycle of the diagram's perimeter corresponds to the production of 1 ADP and the ejection of a maximum of 3  $\text{H}^+$ , as driven by the hydrolysis of 1 ATP by the  $\text{F}_1\text{F}_0$ -ATPase in the mitochondrial inner membrane. The pump functions in the reverse direction in vivo. Further details appear in the text.

etry of 3  $\text{H}^+$  translocated for each ATP hydrolyzed or synthesized is consistent with current estimates (24).

The parameter set for the proton pump diagram (Table 3 and APPENDIX B) differs from that used to describe respiration-driven proton ejection in that the rate constants now favor flux reversal at lower values of the reaction force, which, here, is the matrix phosphorylation potential. (This is especially true of the settings for the  $\Delta\Psi$ -dependent  $1 \leftrightarrow 6$  transitions, as well as for the  $4 \leftrightarrow 5$  and  $5 \leftrightarrow 6$  pairs that affect the orientation of the  $\text{H}^+$ -loaded complex and the net binding rate for cytosolic protons.) The rate constants that determine slippage ( $2 \leftrightarrow 5$ ) are representative of an incompletely coupled ATP-hydrolyzing pump.

Table 3. $\text{F}_1\text{F}_0$ -ATPase-driven $\text{H}^+$ pump parameters			
Quantity		Value	Reference
$K_{F1}$	Equilibrium constant for Eq. 11	$1.71 \times 10^6 \text{ mM}$	52
$[\text{ADP}]_{m,\text{free}}$	Not bound to fixed sites	$0.8 [\text{ADP}]_m$	41
$[\text{P}_i]_m$	Matrix phosphate concentration	20 mM	39
$\rho_{F1}$	$\text{H}^+$ pump concentration	0.7 nmol/mg protein	5, 65
$p_1$	Sum of $\alpha_i$ products	$1.346 \times 10^{-8}$	40, 52
$p_2$	Sum of $\alpha_i$ products	$7.739 \times 10^{-7}$	40, 52
$p_3$	Sum of $\alpha_i$ products	$6.65 \times 10^{-15}$	40, 52
$p_a$	Sum of $\alpha_i$ products	$1.656 \times 10^{-5}/\text{s}$	40, 52
$p_b$	Sum of $\alpha_i$ products	$3.373 \times 10^{-7}/\text{s}$	40, 52
$p_{c1}$	Sum of $\alpha_i$ products	$9.651 \times 10^{-14}/\text{s}$	40, 52
$p_{c2}$	Sum of $\alpha_i$ products	$4.845 \times 10^{-19}/\text{s}$	40, 52
$\Delta\Psi_B$	Total phase boundary potentials	50 mV	52

See APPENDIX B and Eq. 13.

No changes have been made to the Pietrobon-Caplan model of the  $\text{F}_1\text{F}_0$ -ATPase (52), although its properties are modified because of the adenine nucleotide conservation condition in the  $\beta$ -cell model (Eq. 10) (40). Pietrobon and Caplan use a unimolecular rate constant for the  $4 \rightarrow 3$  binding of ADP and  $\text{P}_i$ , assuming fixed concentrations of 20  $\mu\text{M}$  and 10 mM, respectively. Changing the matrix phosphate concentration to 20 mM (39) and allowing  $[\text{ADP}]_m$  to vary gives a product equal to the original rate constant value for  $[\text{ADP}]_{m,\text{free}} = 125 \mu\text{M}$ . Without an upper limit on  $[\text{ATP}]_m$ , its high settings as a parameter can produce the elevated

Table 4. Adenine nucleotide translocator parameters

	Quantity	Value	Reference
$J_{\text{max,ANT}}$	Maximum exchange rate, $\text{ADP}_i - \text{ADP}_m$	$1,000 \text{ nmol} \cdot \text{min}^{-1} \cdot \text{mg protein}^{-1}$	29, 65
$[\text{ADP}^{3-}]_m$	$0.45 [\text{ADP}]_{m,\text{free}}$	$0.45 \cdot 0.8 \cdot [\text{ADP}]_m$	12
$[\text{ADP}^{3-}]_i$	$0.45 [\text{ADP}]_{i,\text{free}}$	$0.45 \cdot 1.0 \cdot [\text{ADP}]_i$	12
$[\text{ATP}^{4-}]_m$		$0.05 \cdot [\text{ATP}]_m$	12
$[\text{ATP}^{4-}]_i$		$0.05 \cdot [\text{ATP}]_i$	12
$f$	Fraction effective $\Delta\Psi$	0.5	6

multiple catalytic sites on the ATPase (4). The ATP production rate is then

$$J_{\text{p,F1}} = -60\rho_{\text{F1}} \frac{\left[ p_a 10^{3\Delta\text{pH}} + p_{c1} \exp\left(\frac{3F\Delta\Psi_B}{RT}\right) \right] \exp\left(\frac{FA_{\text{F1}}}{RT}\right) - p_a \exp\left(\frac{3F\Delta\Psi}{RT}\right) + p_{c2} \exp\left(\frac{FA_{\text{F1}}}{RT}\right) \exp\left(\frac{3F\Delta\Psi}{RT}\right)}{\left[ 1 + p_1 \exp\left(\frac{FA_{\text{F1}}}{RT}\right) \right] \exp\left(\frac{3F\Delta\Psi_B}{RT}\right) + \left[ p_2 + p_3 \exp\left(\frac{FA_{\text{F1}}}{RT}\right) \right] \exp\left(\frac{3F\Delta\Psi}{RT}\right)} \quad (13)$$

phosphorylation potentials associated with ADP production and  $\text{H}^+$  ejection. However, the conservation condi-

The  $\text{H}^+$  uptake rate includes a factor of 3 corresponding to the ideal  $\text{H}^+:\text{P}_i$  ratio (24)

$$J_{\text{H,F1}} = -180\rho_{\text{F1}} \frac{p_a 10^{3\Delta\text{pH}} \exp\left(\frac{FA_{\text{F1}}}{RT}\right) - [p_a + p_b] \exp\left(\frac{3F\Delta\Psi}{RT}\right)}{\left[ 1 + p_1 \exp\left(\frac{FA_{\text{F1}}}{RT}\right) \right] \exp\left(\frac{3F\Delta\Psi_B}{RT}\right) + \left[ p_2 + p_3 \exp\left(\frac{FA_{\text{F1}}}{RT}\right) \right] \exp\left(\frac{3F\Delta\Psi}{RT}\right)} \quad (14)$$

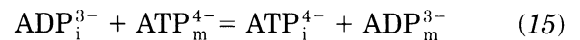
tion in Eq. 10 used here limits the  $2 \rightarrow 3$  transition rate, making our simulated ATP hydrolysis rates up to an order of magnitude lower (52). As the simulation of oxidative phosphorylation is not significantly affected and reversal of  $\text{F}_1\text{F}_0$ -ATPase activity does not occur in vivo under normal conditions, further adjustments to the Pietrobon-Caplan parameter set needed for dealing with this problem have not been pursued.

The steady-state expressions produced by diagrammatic methods for the coupled reactions mediated by the  $\text{F}_1\text{F}_0$ -ATPase can be reduced to expressions similar to those in Eqs. 5 and 6 (40). As in the model for the respiration-driven proton pump, the new parameters  $p$  (Table 3 and APPENDIX B) depend only on the fixed factors of the original Pietrobon-Caplan rate constants. The driving reaction (Eq. 11) has equilibrium constant  $K_{\text{F1}}$  and affinity

$$A_{\text{F1}} = \frac{RT}{F} \ln \left( \frac{K_{\text{F1}}[\text{ATP}]_m}{[\text{ADP}]_{m,\text{free}}[\text{P}_i]_m} \right) \quad (12)$$

where the value of  $K_{\text{F1}}$  reflects the matrix pH and  $\text{Mg}^{2+}$  content. We use a pump density  $\rho_{\text{F1}} = 0.7 \text{ nmol/mg protein}$  that is somewhat higher than the measured concentration of the  $\text{F}_1\text{F}_0$ -ATPase in liver mitochondria (0.1–0.4 nmol/mg protein) (5, 65) (see Table 4). This higher value may be due to the concurrent action of

Although adenine nucleotide translocator activity has been observed in islet tissue (68), the carrier has been studied more extensively in heart and liver mitochondria. A sequential mechanism has been proposed by Bohnensack (6) in which oppositely oriented sites bind either  $\text{ATP}^{4-}$  or  $\text{ADP}^{3-}$ , and both sites must be filled before the protein isomerization that causes a ligand exchange across the inner membrane can occur (Fig. 5A). Since the binding sites accept either species, four different carrier-ligand complexes are possible, each with its corresponding rates for the exchange and unbinding of a different adenine nucleotide pair. The membrane polarization of energized mitochondria favors the translocation reaction



which has been shown to reach a Nernstian equilibrium (30).

On the basis of this mechanism, as well as on other properties of the carrier, Bohnensack has developed a rate law for adenine nucleotide translocator activity (6), which alternatively can be derived from the Altman-King-Hill diagram of Fig. 5B (40). The final expression for the exchange flux of  $\text{ADP}_i$  and  $\text{ATP}_m$  ( $J_{\text{ANT}}$ ) includes a parameter  $f = 0.5$  for the fraction of  $\Delta\Psi$  responsible for the large increase in the Michaelis-Menten constant ( $K_m$ ) for ATP uptake by energized mitochondria, and a factor  $J_{\text{max,ANT}} =$

1,000  $\text{nmol} \cdot \text{min}^{-1} \cdot \text{mg protein}^{-1}$  for the maximum rate for  $\text{ADP}_i/\text{ADP}_m$  exchange in the absence of ATP (29, 65)

$$J_{\text{ANT}} =$$

$$J_{\text{max,ANT}} \frac{1 - \frac{[\text{ATP}^{4-}]_i [\text{ADP}^{3-}]_m}{[\text{ADP}^{3-}]_i [\text{ATP}^{4-}]_m} \exp\left(\frac{-F\Delta\Psi}{RT}\right)}{\left\{1 + \frac{[\text{ATP}^{4-}]_i}{[\text{ADP}^{3-}]_i} \exp\left(\frac{-fF\Delta\Psi}{RT}\right)\right\} \left\{1 + \frac{[\text{ADP}^{3-}]_m}{[\text{ATP}^{4-}]_m}\right\}} \quad (16)$$

The fluxes in *Eqs. 13 and 16* define the rate of change of  $[\text{ADP}]_m$  in the matrix

$$\frac{d[\text{ADP}]_m}{dt} = J_{\text{ANT}} - J_{\text{p,F1}} \quad (17)$$

where ATP production by substrate level phosphorylation in the mitochondria has been neglected. Adding

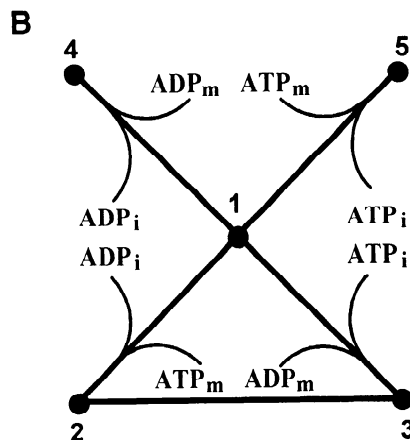
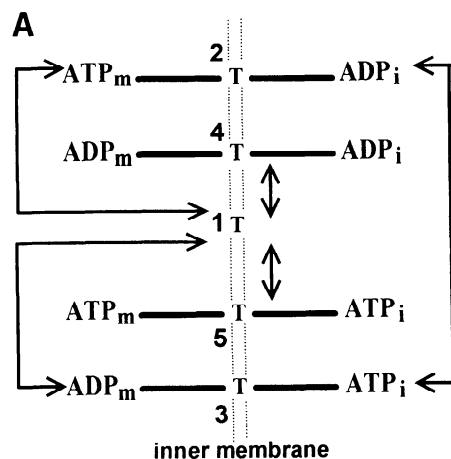


Fig. 5. A: sequential mechanism for the mitochondrial adenine nucleotide translocator (T), showing all possible states and the allowed transitions between them. Binding of either  $\text{ATP}^{4-}$  or  $\text{ADP}^{3-}$  must occur to sites on both sides of the inner membrane before isomerization of the carrier protein results in an exchange of the ligands. State 1 is unoccupied. B: equivalent Altman-King-Hill diagram. Subscript m, mitochondrial; subscript i, cytosolic.

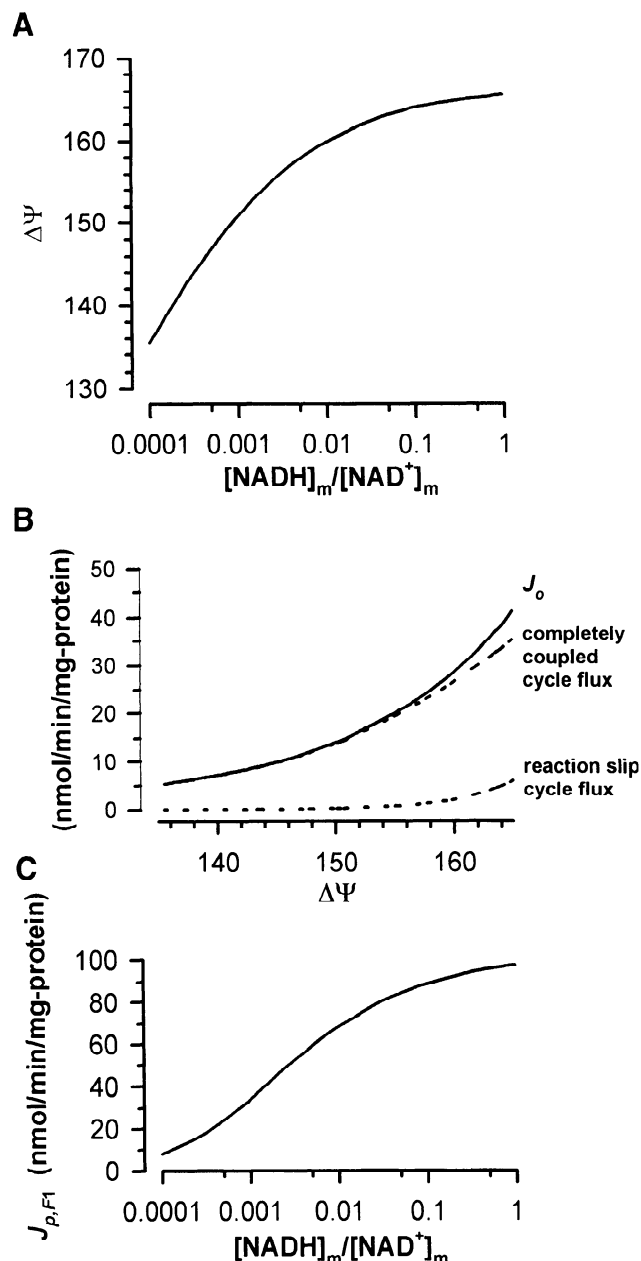


Fig. 6. Steady-state characteristics of state 3 mitochondria with blocked  $\text{Ca}^{2+}$  transport and external  $\text{ATP}/\text{ADP} = 4$ , as simulated using *Eqs. 17–18*. A: the membrane voltage  $\Delta\Psi$  saturates at a lower value than in state 4, because of the depolarization caused by  $\text{H}^+$  uptake through the active  $\text{F}_1\text{F}_0$ -ATPase. B: the lower  $\Delta\Psi$  also greatly diminishes the contribution of reaction slip cycle flux to the oxygen consumption rate compared with static head conditions (Fig. 3), although the diminished respiratory control also more than doubles  $J_{\text{O}_2}$ . C: dependence of the ATP production rate ( $J_{\text{p,F1}}$ ) on the matrix  $[\text{NADH}]_m/[\text{NAD}^+]_m$  ratio.

the currents given by the same equations to *Eq. 8* yields

$$C_{\text{mito}} \frac{d\Delta\Psi}{dt} = -(-J_{\text{H,res}} + J_{\text{H,F1}} + J_{\text{ANT}} + J_{\text{H,leak}}) \quad (18)$$

We use *Eqs. 17 and 18* to describe state 3 mitochondria. The steady-state membrane potential is determined by setting the *left* sides of *Eqs. 17 and 18* equal to zero and solving for  $\Delta\Psi$  as a function of  $[\text{NADH}]_m$ .



The results in Fig. 6, A and B, show the increases in  $\Delta\Psi$  and the oxygen consumption rate,  $J_o$ , predicted by the model. Note the leveling of  $\Delta\Psi$  as the matrix  $[\text{NADH}]_m:[\text{NAD}^+]_m$  ratio is raised parametrically up to a maximal state 3 level near a value of 1. The changes in these variables are greater than the corresponding state 4 increases (Fig. 3, A and B). The higher oxygen consumption rates and lower membrane potentials for state 3 compared with state 4 in Fig. 3 are generally consistent with experiments on phosphorylating and nonphosphorylating mitochondria in rat hepatocytes (14, 19). In the simulation the reaction slip contribution to  $J_o$  is much lower in state 3 than in state 4 (compare Figs. 3B and 6B), because of the lower membrane potential in state 3 (52). The simulated rate of ATP production has an inflected region for  $[\text{NADH}]_m/[\text{NAD}^+]_m$  between 0.001 and 0.01, values typical of liver mitochondria in vivo (15). In these simulations  $[\text{ATP}]_m:[\text{ADP}]_m$  ratios remain near 1, decreasing to about 0.4 as  $[\text{NADH}]_m/[\text{NAD}^+]_m$  approaches 0.001.

### CALCIUM HANDLING BY MITOCHONDRIA

In the pancreatic  $\beta$ -cell the two major  $\text{Ca}^{2+}$  influx and efflux pathways through the inner mitochondrial membrane are the  $\text{Ca}^{2+}$  uniporter (influx) and the  $\text{Na}^+/\text{Ca}^{2+}$  exchanger (efflux) (17, 18). Here we describe kinetic models of these two transport mechanisms and select kinetic parameters to match experimental data. Although a preponderance of evidence suggests that the  $\text{Na}^+/\text{Ca}^{2+}$  exchanger is electroneutral (2:1 stoichiometry) (7, 18, 67), we also investigate the consequences of making the transport electrogenic (3:1 stoichiometry) (3). Buffering of  $\text{Ca}^{2+}$  ions is another important feature of  $\text{Ca}^{2+}$  handling, and we take this into account as well.

The  $\text{Ca}^{2+}$  uniporter is a pathway for  $\text{Ca}^{2+}$  influx whose rate is dependent on the  $\text{Ca}^{2+}$  concentration external to the matrix,  $[\text{Ca}^{2+}]_i$ , and the inner membrane potential,  $\Delta\Psi$  (17, 18). To describe the dependence of the rate on these quantities, we use the allosteric model in Fig. 7. That model is inspired by steady-state measurements of  $\text{Ca}^{2+}$  uptake into liver mitochondria that exhibit Hill coefficients ranging from 2 to 3.5, depending on experimental conditions (35). We rely on the diagram in Fig. 7 to obtain an analytic

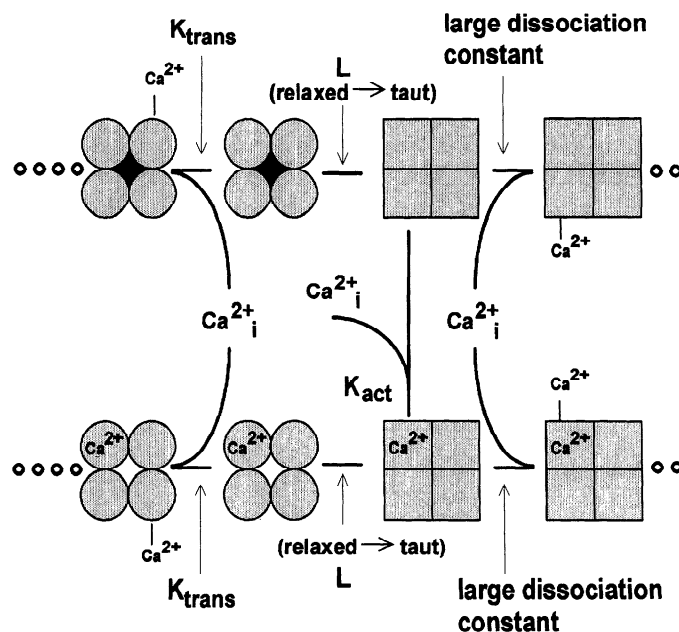


Fig. 7. Allosteric mechanism for the  $\text{Ca}^{2+}$ -dependence of the  $\text{Ca}^{2+}$  uniporter, where the binding of "activating"  $\text{Ca}^{2+}$  is shown as internal and that of "transported"  $\text{Ca}^{2+}$  as external to the 4 protomers of the regulatory sector. Further details appear in the text.

Two types of binding sites for  $\text{Ca}^{2+}$  are believed to exist on the uniporter, one which is associated with the transport process and another that activates the uniporter (33, 34). It is assumed that each subunit in the model can bind one "activating"  $\text{Ca}^{2+}$  and one "transported"  $\text{Ca}^{2+}$ , with dissociation constants indicated by  $K_{\text{act}}$  and  $K_{\text{trans}}$ , respectively. The unactivated relaxed states are in the *top left* of the diagram in Fig. 7, whereas the activated relaxed states are in the *bottom left*. Only the activated relaxed states are assumed to be involved in transport. Those states with transportable  $\text{Ca}^{2+}$  ions bound contribute to the rate in proportion to the number of bound ions.

The rate of the uniporter is a product of three factors: a maximal rate ( $J_{\text{max,uni}}$ ); the fractional saturation of the uniporter by transportable  $\text{Ca}^{2+}$ ; and a mitochondrial membrane potential term that we approximate here using a constant-field-type approximation. Analyzing the allosteric model in the usual way (48) gives

$$J_{\text{uni}} = J_{\text{max,uni}} \cdot \frac{\frac{[\text{Ca}^{2+}]_i}{K_{\text{trans}}} \left(1 + \frac{[\text{Ca}^{2+}]_i}{K_{\text{trans}}}\right)^3}{\left(1 + \frac{[\text{Ca}^{2+}]_i}{K_{\text{trans}}}\right)^4 + \frac{L}{\left(1 + \frac{[\text{Ca}^{2+}]_i}{K_{\text{act}}}\right)^{n_a}}} \cdot \frac{2F(\Delta\Psi - \Delta\Psi^*)}{RT} \cdot \frac{1 - \exp\left\{\frac{-2F(\Delta\Psi - \Delta\Psi^*)}{RT}\right\}}{1} \quad (19)$$

expression for the uptake rate and adjust model parameters to fit the steady-state experiments.

Figure 7 treats the uniporter as consisting of four equivalent binding domains that can exist in either a "relaxed" (all circles) or "taut" (all squares) form. The allosteric constant for this transition is indicated as  $L$ .

In this equation we have adopted the activation cooperativity parameter,  $n_a = 2.8$ , which comes from the work of Kröner (34), and have introduced the parameter  $\Delta\Psi^* = 91$  mV, used in previous work by Gunter and colleagues (66) to account for the potential profile within the pore of the uniporter.

Spermine, which is abundant in  $\beta$ -cells (23), is known to bind to and activate the uniporter (35). In our allosteric model this can be taken into account by lowering  $L$ . To compare experimental measurements with mitochondrial preparations, however, we have adopted a higher value than that used in our whole  $\beta$ -cell calculations. The value of  $K_{\text{act}}$  is taken from the work of Kröner (34), whereas the values of  $K_{\text{trans}}$ ,  $L$ , and  $J_{\text{max,uni}}$  were taken to fit the dependence of the uniporter rate on  $\Delta\Psi$  and  $[\text{Ca}^{2+}]_i$  (Table 5). A comparison of predicted values of  $J_{\text{uni}}$  with data of Gunter and colleagues (66) is shown in Fig. 8. There the symbols

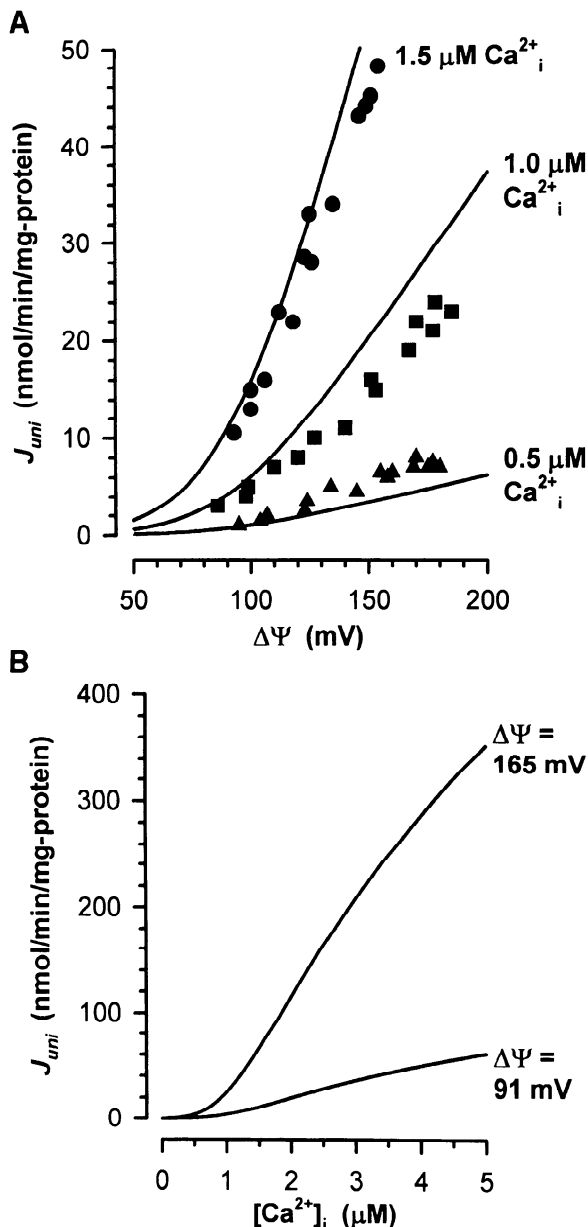


Fig. 8. A: fit of the  $\text{Ca}^{2+}$  uniporter rate law (Eq. 19) to the data of Gunter and colleagues (66), illustrating the dependence of uniporter-mediated  $\text{Ca}^{2+}$  influx ( $J_{\text{uni}}$ ) on the membrane potential for 0.5, 1.0, and 1.5  $\mu\text{M}$  external  $\text{Ca}^{2+}$ . B: simulated dependence of  $J_{\text{uni}}$  on  $[\text{Ca}^{2+}]_i$  at membrane potentials characteristic of deenergized ( $\Delta\Psi = 91 \text{ mV}$ ) and state 3 ( $\Delta\Psi = 165 \text{ mV}$ ) mitochondria.

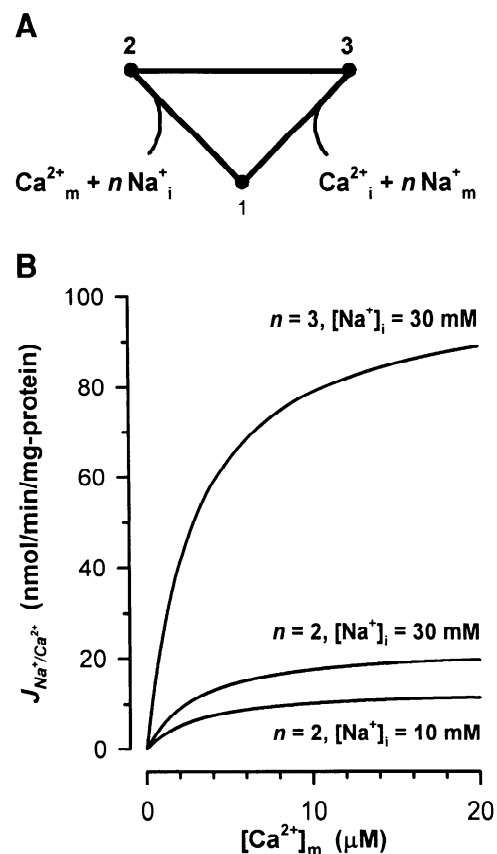


Fig. 9. A: Altman-King-Hill diagram for states of the  $\text{Na}^+/\text{Ca}^{2+}$  exchanger, where the isomerization of the carrier after the binding of 1 matrix  $\text{Ca}^{2+}$  and  $n$  external  $\text{Na}^+$  ( $1 \rightarrow 2 \rightarrow 3$ ) results in the release of these ions on opposite sides of the mitochondrial inner membrane ( $3 \rightarrow 1$ ). B: dependence of mitochondrial  $\text{Ca}^{2+}$  efflux  $J_{\text{Na}^+/\text{Ca}^{2+}}$  on  $[\text{Ca}^{2+}]_m$  is shown for two external  $\text{Na}^+$  concentrations and an electroneutral carrier ( $n = 2$ ), and the effect of an electrogenic exchange on  $J_{\text{Na}^+/\text{Ca}^{2+}}$  ( $n = 3$ ) is illustrated by the top curve.

represent measurements of the rate of the uniporter in nanomoles per minute per milligram protein as a function of inner membrane potential for three different values of  $[\text{Ca}^{2+}]_i$ . The theoretical curves are in reasonable agreement with the experiment, reproducing quantitatively the increase in rate both with  $\Delta\Psi$  and  $[\text{Ca}^{2+}]_i$  throughout the physiological regime.

To represent efflux of  $\text{Ca}^{2+}$  through the  $\text{Na}^+/\text{Ca}^{2+}$  exchanger found in the mitochondria of excitable cells, we use the scheme diagrammed in Fig. 9A. The transition between states 1 and 2 represents the binding of a  $\text{Ca}^{2+}$  ion from the mitochondrial matrix and  $n$   $\text{Na}^+$  ions from outside the inner membrane. The transition  $2 \rightarrow 3$  is the exchange step, whereas the transition  $3 \rightarrow 1$  releases a single  $\text{Ca}^{2+}$  outside and  $n$   $\text{Na}^+$  ions in the matrix. The exchanger is electroneutral if  $n = 2$  and electrogenic if  $n = 3$ . Although recent evidence suggests that the mitochondrial exchanger is electroneutral (7, 18, 67), we also have examined the consequences of assuming that the exchanger is electrogenic (3). For simplicity, we have assumed that the three states of the exchanger in the diagram rapidly equilibrate to the local concentrations of  $\text{Na}^+$  and  $\text{Ca}^{2+}$ . Although mito-

Table 5. Mitochondrial  $\text{Ca}^{2+}$  handling parameters

	Quantity	Value	Reference
$J_{\text{max,uni}}$	Uniporter maximum rate, $\Delta\Psi = \Delta\Psi^*$	$300 \text{ nmol} \cdot \text{min}^{-1} \cdot \text{mg protein}^{-1}$	33
$K_{\text{trans}}$	$K_d$ for uniporter translocated $\text{Ca}^{2+}$	$19 \mu\text{M}$	18
$K_{\text{act}}$	$K_d$ for uniporter activating $\text{Ca}^{2+}$	$0.38 \mu\text{M}$	34
$n_a$	Uniporter activation cooperativity	2.8	34
$L$	$K_{\text{eq}}$ for uniporter conformations	110 (adjusted)	
$\Delta\Psi^*$	$\Delta\Psi$ offset for $\text{Ca}^{2+}$ transport	91 mV	66
$J_{\text{max,Na}^+/\text{Ca}^{2+}}$	$\text{Na}^+/\text{Ca}^{2+}$ exchanger maximum rate, $\Delta\Psi = \Delta\Psi^*$	$25 \text{ nmol} \cdot \text{min}^{-1} \cdot \text{mg protein}^{-1}$	55
$b$	$\text{Na}^+/\text{Ca}^{2+}$ exchanger $\Delta\Psi$ dependence	0 (adjusted)	
$K_{\text{Na}}$	$K_m(\text{Na}^+)$ for $\text{Na}^+/\text{Ca}^{2+}$ exchanger	9.4 mM	9
$K_{\text{Ca}}$	$K_m(\text{Ca}^{2+})$ for $\text{Na}^+/\text{Ca}^{2+}$ exchanger	$0.003 \text{ nmol/mg protein}$	11, 67
$[\text{Na}^+]_i$		30 mM	2
$f_m$	Fraction free matrix $\text{Ca}^{2+}$	0.0003	11

$K_d$ , dissociation constant;  $K_{\text{eq}}$ , equilibrium constant;  $K_m$ , Michaelis-Menten constant.

chondrial concentrations of  $\text{Na}^+$  have not been measured directly, we can take advantage of the rapid  $\text{H}^+/\text{Na}^+$  exchange to estimate that free mitochondrial sodium concentrations ( $[\text{Na}^+]_m$ ) are a function of the pH gradient (13) and therefore at least a factor of 3 smaller than typical cytosolic values ( $[\text{Na}^+]_i \approx 30 \text{ mM}$  in the  $\beta$ -cell; Ref. 2). This, along with the fact that exchanger-mediated uptake of  $\text{Ca}^{2+}$  is not observed experimentally, allows us to set the transition rate for the step  $1 \rightarrow 3$  equal to zero.

The rate of exchange for the diagram in Fig. 9A is determined by the rate of the exchange step,  $2 \rightarrow 3$ . This is defined by the intrinsic rate of the process,  $\Omega$ , multiplied by a thermodynamic factor that takes into account the probability that the forward and reverse steps occur (27)

$$J_{\text{Na}^+/\text{Ca}^{2+}} = \Omega \left[ \exp\left(\frac{\mu_2}{RT}\right) - \exp\left(\frac{\mu_3}{RT}\right) \right] \quad (20)$$

where the  $\mu_2$  and  $\mu_3$  are the electrochemical potentials of states 2 and 3, respectively. Assuming the usual relationship between the electrochemical potentials and the fraction of channels in states 2 and 3, we are led to the following formula for the  $\text{Na}^+/\text{Ca}^{2+}$  exchange rate

$$J_{\text{Na}^+/\text{Ca}^{2+}} = J_{\text{max,Na}^+/\text{Ca}^{2+}} \frac{\exp\left\{\frac{bF(\Delta\Psi - \Delta\Psi^*)}{RT}\right\}}{\left(1 + \frac{K_{\text{Na}}}{[\text{Na}^+]_i}\right)^n \left(1 + \frac{K_{\text{Ca}}}{[\text{Ca}^{2+}]_m}\right)} \quad (21)$$

Here  $J_{\text{max,Na}^+/\text{Ca}^{2+}}$  is the maximum rate when  $\Delta\Psi = \Delta\Psi^*$ , i.e., under uncoupled conditions. For simplicity we take the same value of  $\Delta\Psi^* = 91 \text{ mV}$  that we have used for the pore correction to the uniporter potential. Expressions similar to this have been used to describe the rate of  $\text{Na}^+/\text{Ca}^{2+}$  exchangers, and we have adopted experimental values for the dissociation constants,  $K_{\text{Na}}$  and  $K_{\text{Ca}}$  (9, 11, 67). The kinetic parameters are listed in Table 5.

Figure 9B exhibits the dependence of the rate,  $J_{\text{Na}^+/\text{Ca}^{2+}}$ , on  $[\text{Ca}^{2+}]_m$  and  $[\text{Na}^+]_i$  for the electroneutral case,  $n = 2$ .

In this case  $b = 0$  and there is no dependence on the membrane potential. As shown in Fig. 9B, small variations of  $[\text{Na}^+]_i$  in the physiological range make small changes in the rate, whereas the dependence on  $[\text{Ca}^{2+}]_m$  is hyperbolic. For  $n = 3$  the exchanger is electrogenic. If we set  $b = 0.5$ , the rate of the exchanger is greatly increased when all other parameters are fixed. This is illustrated in Fig. 9B for  $[\text{Na}^+]_i = 30 \text{ mM}$  and  $\Delta\Psi = 165 \text{ mV}$ . Because the dependence of the rates in the model on  $\Delta\Psi$  has been assumed to arise only from the transition between 2 and 3, if neither  $[\text{Na}^+]_i$  nor the membrane potential changes appreciably, then their effect can be factorized into the parameter  $J_{\text{max,Na}^+/\text{Ca}^{2+}}$ . In the remaining sections we consider only the electro-neutral case.

Fixed  $\text{Ca}^{2+}$  binding sites reduce the concentration of free  $\text{Ca}^{2+}$  in the mitochondrial matrix, probably even beyond that due to  $\text{Ca}^{2+}$  buffers in the cytoplasm. It is likely that  $\text{Ca}^{2+}$  buffering is responsible for the relatively low values of free  $\text{Ca}^{2+}$  reported by fluorescent indicators under resting conditions (about  $0.2 \mu\text{M}$ ; Ref. 56). Whereas resting total  $\text{Ca}^{2+}$  concentrations ranging from 0.5 to as high as  $10 \text{ nmol/mg protein}$  have been reported in cardiac and liver mitochondria (11, 60, 66), unbound matrix  $\text{Ca}^{2+}$  concentrations are generally three orders of magnitude lower (26). Evidence from “inside-out” submitochondrial particles suggests that much of this binding may be at the inner leaflet of the inner membrane (59). Here we use a constant value of  $f_m = 0.0003$  (0.03%) for the fraction of total  $\text{Ca}^{2+}$  that is free in the matrix. This is a rough average of values reported for rat liver and heart mitochondria (11).

Two other  $\text{Ca}^{2+}$  handling mechanisms may be important in mitochondria under certain conditions, i.e., the precipitation of  $\text{Ca}^{2+}$  in the form of  $\text{Ca}_3(\text{PO}_4)_2$  and the permeability transition pore (17). We consider neither of these processes here, since there is no evidence that either of these processes is important in the  $\beta$ -cell under normal physiological conditions. We also have neglected a second, rapid  $\text{Ca}^{2+}$  uptake pathway recently discovered by Gunter and colleagues (61). We refer the interested reader to the relevant literature for further information.

## FULL MINIMAL MODEL

The full minimal model includes dynamic changes in the mitochondrial membrane potential and mitochondrial ADP and  $\text{Ca}^{2+}$  concentrations. Introducing the balance equation for  $[\text{Ca}^{2+}]_m$  based on the fluxes in the previous section, we show the equations for the full model to be

$$\frac{d[\text{Ca}^{2+}]_m}{dt} = f_m(J_{\text{uni}} - J_{\text{Na}^+/\text{Ca}^{2+}}) \quad (22)$$

$$\frac{d[\text{ADP}]_m}{dt} = (J_{\text{ANT}} - J_{\text{p,F1}}) \quad (23)$$

$$C_{\text{mito}} \frac{d\Delta\Psi}{dt} = -(-J_{\text{H,res}} + J_{\text{H,F1}} + J_{\text{ANT}} + J_{\text{H,leak}} + 2J_{\text{uni}}) \quad (24)$$

These equations are used to simulate both steady-state and transient responses of all three variables and the fluxes. An electronic file, formatted for the ordinary differential equation analysis package, Xppaut, can be found in the *Gallery of Models* (<http://www.itd.ucdavis.edu/>).

Simulated steady-state values of  $\Delta\Psi$ ,  $J_o$ , and  $J_{\text{p,F1}}$  as functions of  $[\text{Ca}^{2+}]_i$  up to  $5 \mu\text{M}$  are shown in Fig. 10. There, state 3 is defined by saturating external ADP and fixed equal NADH and  $\text{NAD}^+$  concentrations, and state 4 is defined by 99% reduced NAD (63). The results generated by the model are consistent quantitatively with state 4 experiments, whereas the simulations for state 3 show fluxes about one-half as great as have been observed for succinate-fueled mitochondrial preparations (49).

As seen in Fig. 8, the uniporter-mediated  $\text{Ca}^{2+}$  influx declines as the membrane depolarizes, with the rate of this decrease higher at the larger external  $\text{Ca}^{2+}$  concentrations. The more polarized the membrane, the greater the  $\text{Ca}^{2+}$  influx, but also the stronger the effect of  $J_{\text{uni}}$  on the rate at which  $\Delta\Psi$  is lowered (Eq. 24). In Fig. 10A the steep drop in the state 4 membrane potential at values of  $[\text{Ca}^{2+}]_i$  above about  $0.5 \mu\text{M}$  is due to the strong effect of such large  $J_{\text{uni}}$  currents in depolarizing the membrane. The smaller values of  $\Delta\Psi$  then rapidly reduce the flux, despite the high levels of  $[\text{Ca}^{2+}]_i$ . As seen by the *bottom* curve of Fig. 10A, the reductions in  $\Delta\Psi$  predicted for  $\text{Ca}^{2+}$  added to state 3 mitochondria are much smaller. The lower  $\Delta\Psi$  results from the  $\text{H}^+$  cycling during phosphorylation, whereas its decline with increasing  $[\text{Ca}^{2+}]_i$  is associated with lower  $\text{Ca}^{2+}$  fluxes and hence with smaller changes in the inner membrane potential.

The simulation of  $J_o$  in state 4 shown in Fig. 10B is in agreement with the increased oxygen consumption following  $\text{Ca}^{2+}$  additions to nonphosphorylating rat heart and liver mitochondria (25, 49). Experimentally, the inflected region near  $0.5 \mu\text{M}$  has been shown to depend on the presence of  $\text{Mg}^{2+}$  and other effectors of the  $\text{Ca}^{2+}$  uniporter. A comparable increase in  $J_o$  occurs in the simulation of state 3 mitochondria (Fig. 10B).

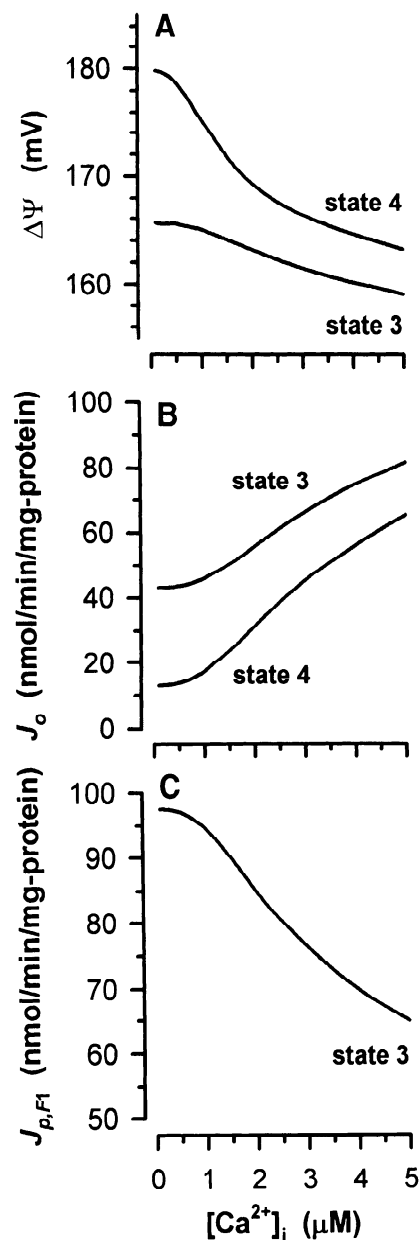


Fig. 10. Steady-state fluxes in phosphorylating and nonphosphorylating mitochondria as simulated using the full minimal model (Eqs. 22–24). State 4 simulations have the  $[\text{NADH}]_m:[\text{NAD}^+]_m$  ratio fixed at 100 and the  $\text{F}_1\text{F}_0$ -ATPase activity blocked ( $\rho_{\text{F1}} = 0$ ), whereas state 3 corresponds to  $[\text{NADH}]_m:[\text{NAD}^+]_m = 1$  and  $[\text{ATP}]_i/[\text{ADP}]_i = 4$ . Dependence on the external  $\text{Ca}^{2+}$  concentration is shown for the membrane potential  $\Delta\Psi$  (A), oxygen consumption  $J_o$  (B), and ATP production  $J_{\text{p,F1}}$  (C).

Although the rise in  $J_o$  is less than that observed experimentally, the results still capture the complexity of state 3 conditions at submicromolar values of  $[\text{Ca}^{2+}]_i$  (49).

Both the experimental and simulated oxygen uptake by state 3 mitochondria increase with the concentration of added  $\text{Ca}^{2+}$ ; however, the decline in  $J_o$ , observed experimentally for  $[\text{Ca}^{2+}]_i$  above about  $1.0 \mu\text{M}$  (49), is not seen in the simulation. This comparison with experiment is somewhat misleading because the experimental transients of NADH oxidation observed immedi-

ately after fixed additions of ADP or  $\text{Ca}^{2+}$  to state 4 mitochondria (10) are not included in the minimal model. A more realistic model, such as we use to treat the whole  $\beta$ -cell, would include both the stimulatory effect of the mitochondrial dehydrogenases and the change in the  $[\text{NADH}]_m/[\text{NAD}^+]_m$  ratio due to oxidation. Reductions in the respiratory driving force resulting from increased substrate oxidation rates are likely to rise with the size of the  $\text{Ca}^{2+}$  additions. High external  $\text{Ca}^{2+}$  concentrations would then tend to lower  $\Delta\Psi$  to a greater extent than can be simulated in the current minimal model. A collapsed membrane voltage in combination with a low respiratory driving force should drastically lower  $J_o$ , eventually deenergizing the system. The decline of  $J_o$  does not occur in state 4 mitochondria, because the inner membrane is initially more polarized and the matrix NAD almost entirely in its reduced state.

Because  $[\text{NADH}]_m$  is assumed constant, we are unable to simulate the stimulation of key metabolic dehydrogenases in the matrix by submicromolar levels of sequestered free  $\text{Ca}^{2+}$ . The resulting increase in the rate of production of NADH raises the  $[\text{NADH}]_m/[\text{NAD}^+]_m$  ratio. This positive effect of mitochondrial  $\text{Ca}^{2+}$  uptake on the driving force for respiration has been observed to depend on effectors of mitochondrial  $\text{Ca}^{2+}$  transport and would tend to shift the inflected region of the  $J_o$  curve in Fig. 10B to smaller  $[\text{Ca}^{2+}]_i$  (44). The stimulation of NADH production by low levels of external  $\text{Ca}^{2+}$  may also be implicated in an increase in the rate of ATP synthesis that has been observed in rat liver mitochondria for  $[\text{Ca}^{2+}]_i$  below  $0.5 \mu\text{M}$  (49). The minimal model cannot reproduce this effect or the sudden failure of oxidative phosphorylation that parallels the collapse of state 3 oxygen consumption for buffered  $[\text{Ca}^{2+}]_i$  above  $1.0 \mu\text{M}$ . However, the simulated results of Fig. 10C are still consistent with the lowering of  $J_{p,F1}$  seen at intermediate  $[\text{Ca}^{2+}]_i$  where  $J_o$  is increasing (49).

The large accumulations of free  $\text{Ca}^{2+}$  in the matrix of state 4 heart and liver mitochondria depend on  $[\text{Ca}^{2+}]_i$  much as shown in the simulated curve in Fig. 11 (58). The threshold point at which  $[\text{Ca}^{2+}]_m = [\text{Ca}^{2+}]_i$  (about  $0.4 \mu\text{M}$  in these simulations) can be shifted by manipulations of model parameters that parallel changes to experimental conditions (42, 43). For example, the curve moves to the *right* if higher levels of external  $\text{Na}^+$  stimulate the efflux of matrix  $\text{Ca}^{2+}$  via the  $\text{Na}^+/\text{Ca}^{2+}$  exchanger or if additional  $\text{Mg}^{2+}$  is used to increase the sigmoid dependence of the uniporter on  $[\text{Ca}^{2+}]_i$  ( $L$  in Eq. 19); the opposite effect is produced by allosteric activation by spermine. Although the state 4 simulations are consistent with the large amounts of  $\text{Ca}^{2+}$  that can be sequestered by aerobic mitochondria in the presence of  $[\text{Ca}^{2+}]_i$  above  $1 \mu\text{M}$ , the steep increase of the state 3 curve would be attenuated by the same factors that cause the eventual collapse of the membrane potential and oxygen consumption rate under phosphorylating conditions.

Mitochondria can also sequester large amounts of calcium in response to brief  $\text{Ca}^{2+}$  pulses (57). This is

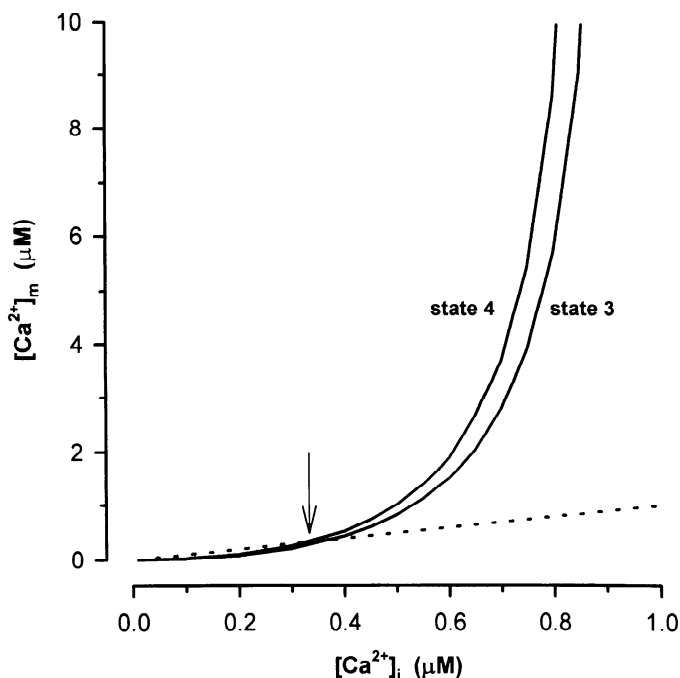


Fig. 11. Dependence of the matrix free  $\text{Ca}^{2+}$  concentration ( $[\text{Ca}^{2+}]_m$ ) on fixed values of  $[\text{Ca}^{2+}]_i$ , as simulated using the full minimal model (Eqs. 22–24), with  $[\text{NADH}]_m/[\text{NAD}^+]_m = 100$  and  $\rho_{F1} = 0$  to block phosphorylation in state 4 and with  $[\text{NADH}]_m/[\text{NAD}^+]_m = 1$  and  $[\text{ATP}]/[\text{ADP}]_i = 4$  for state 3. The curve shifts slightly to the *right* for phosphorylating mitochondria, because of their less polarized membrane and consequently lower uniporter-mediated  $\text{Ca}^{2+}$  uptake rate. Dashed line,  $[\text{Ca}^{2+}]_i = [\text{Ca}^{2+}]_m$ ; arrow, approximate threshold for mitochondrial uptake.

simulated for state 4 in Fig. 12A. The initial elevation of  $[\text{Ca}^{2+}]_i$  that results from the addition of a fixed amount of  $\text{Ca}^{2+}$  ( $0.33 \text{ nmol/mg}$  protein added in a 10-s pulse to a 3-mg protein/ml preparation =  $1 \mu\text{M}$   $\text{Ca}^{2+}$ ) is followed rapidly by a decline to a steady-state level that reflects an accumulation of  $\text{Ca}^{2+}$  in the matrix. Oxygen consumption peaks when the external  $\text{Ca}^{2+}$  is at a maximum and then relaxes to a rate corresponding to a more dissipative level of  $\text{Ca}^{2+}$  cycling across the inner membrane. The changes in oxygen consumption generated by the model are due entirely to the small, transient membrane depolarization that accompanies stimulation of the uniporter and results in a higher steady-state concentration of free  $\text{Ca}^{2+}$  in the matrix (Fig. 12B). The 10-s time course for such an accumulation of mitochondrial  $\text{Ca}^{2+}$  is consistent with recent experiments (61).

## SUMMARY AND CONCLUSIONS

In this work we have developed a minimal model for  $\text{Ca}^{2+}$  handling by mitochondria that includes the basic transport mechanisms summarized in Fig. 1. Because the  $\text{Ca}^{2+}$  uniporter is dependent on mitochondrial membrane potential, the rate of  $\text{Ca}^{2+}$  uptake is dependent on oxidative phosphorylation. Since our long-term interests are in  $\text{Ca}^{2+}$  handling in the pancreatic  $\beta$ -cell, we have modeled oxidation as initiated at complex I and used NADH as the substrate. Oxidation by the respiratory chain influences the membrane potential

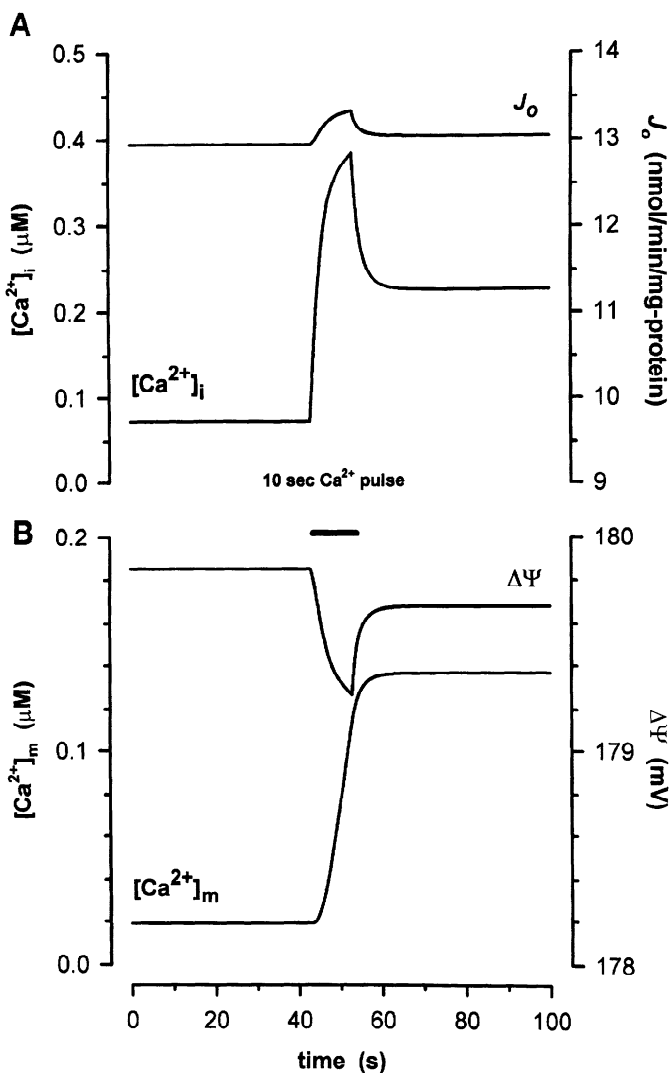


Fig. 12. Effect of a 10-s  $\text{Ca}^{2+}$  pulse with a total concentration of 0.33 nmol/mg protein added to a 3-mg protein/ml preparation of state 4 mitochondria ( $[\text{Ca}^{2+}]_i = 1 \mu\text{M}$ ), as simulated using the full minimal model (Eqs. 22–24), with  $[\text{NADH}]_m/[\text{NAD}^+]_m = 100$  and  $\rho_{\text{F}_1} = 0$  to block phosphorylation. The transient increase in oxygen consumption seen in A is followed by steady-state elevation of  $J_0$  that corresponds to the small amount of external  $\text{Ca}^{2+}$  remaining in the system (top curve). Concurrent dip and steady-state diminishment of the membrane potential  $\Delta\Psi$  (B) also follows the changes in  $[\text{Ca}^{2+}]_i$ , as the matrix free  $\text{Ca}^{2+}$  concentration increases. Total amount of  $\text{Ca}^{2+}$  is conserved in this simulated experiment.

directly via protons pumped out of the matrix and indirectly by establishing the PMF that leads to the influx of protons through the  $\text{F}_1\text{F}_0$ -ATPase. Because the  $\text{F}_1\text{F}_0$ -ATPase uses the PMF to phosphorylate mitochondrial ADP, it is necessary as well to keep track of the transport of ATP and ADP through the mitochondrial inner membrane. Finally, the efflux of  $\text{Ca}^{2+}$  from the matrix is controlled by  $\text{Na}^+/\text{Ca}^{2+}$  exchange, which we have treated here as being electroneutral.

We have developed kinetic models for each of these processes in isolation and have compared them to experimental results using isolated mitochondrial preparations. Parameters, such as concentrations of intermediates and densities of pumps and transporters, have been chosen to correspond with experimental

measurements. To achieve a closer correspondence with metabolism in the pancreatic  $\beta$ -cell, we have modified some of these parameters to reflect metabolic measurements made in pancreatic islets from rat and mice. When combined together, these processes provide a simple description of  $\text{Ca}^{2+}$  handling by mitochondria that involves three time-dependent ordinary differential equations, one for the concentration of  $\text{Ca}^{2+}$  in the mitochondria, another for the mitochondrial membrane potential, and the third for the concentration of ADP in the mitochondrial matrix.

The main features of  $\text{Ca}^{2+}$  handling in the model seem to be in line with experimental measurements. For example, the dependence of the rate of uptake of  $\text{Ca}^{2+}$  by the uniporter on cytosolic  $\text{Ca}^{2+}$  concentration and mitochondrial membrane potential (Fig. 8) are in good agreement with experiments (66). The model also predicts a very sharp increase in the ability of mitochondria to take up  $\text{Ca}^{2+}$  at cytosolic  $\text{Ca}^{2+}$  concentrations of about 0.4–0.5  $\mu\text{M}$  (58). This threshold is not built into the model but, rather, is a consequence of the balancing of the six kinetic processes included in the minimal model. This threshold is particularly sensitive to the balance between the regulated rate of the  $\text{Ca}^{2+}$  uniporter and the  $\text{Na}^+/\text{Ca}^{2+}$  exchange mechanism. Thus increasing the allosteric parameter,  $L$ , for the uniporter to mimic the effect of spermine lowers the threshold, whereas increasing the  $[\text{Na}^+]_i$  increases the threshold. Effects like this are known experimentally (42, 43).

We have been able to achieve good agreement with experiment, despite the fact that we have made a number of simplifying assumptions. First, we have assumed that all of the transporters in Fig. 1 operate under steady-state conditions. This means, for example, that the rate of binding of ATP, ADP,  $\text{Ca}^{2+}$ , etc., to the transport proteins is assumed to be rapid with respect to changes caused by the transporters. Other assumptions, which we have argued are appropriate for the pancreatic  $\beta$ -cell, include fixed total NAD in the matrix, fixed concentration of cytoplasmic  $\text{Na}^+$ , and fixed pH difference between the matrix and the cytosol. Finally, we have assumed that the fraction of free adenine nucleotide intermediates and the fraction of free  $\text{Ca}^{2+}$  in the matrix and cytosol are fixed quantities. Although we believe that these simplifying assumptions are all reasonable, one or more of them may break down under high  $\text{Ca}^{2+}$  loads. Since it is our intention to produce a minimal model that, nonetheless, reflects major  $\text{Ca}^{2+}$  handling mechanisms of mitochondria, we leave further development to future work.

Another important influence of  $\text{Ca}^{2+}$  on mitochondria, which we have not included in the minimal model, is the activation of mitochondrial dehydrogenases. In fact, activation of pyruvate dehydrogenase (PDH) upon D-glucose stimulation has been documented experimentally in pancreatic islets, for which the presumed cause is the increase in cytosolic  $\text{Ca}^{2+}$  concentration (45). We have included the activation of PDH as part of our treatment of electrical activity in the  $\beta$ -cell (40).

Two features of our simulations have important implications for the roles of mitochondria in pancreatic

$\beta$ -cell electrical activity. First, in agreement with recent measurements on INS-1 cells (57), we find that mitochondria are capable of taking up large amounts of  $\text{Ca}^{2+}$ . Pulses of increased  $\text{Ca}^{2+}$  in our simulations (Fig. 12) raise mitochondrial  $\text{Ca}^{2+}$  concentrations on a time scale of 5–10 s. In our steady-state calculations, mitochondrial  $\text{Ca}^{2+}$  readjusts itself to a dynamic steady state that depends on the cytosolic  $\text{Ca}^{2+}$  concentration. Measurements using aequorin targeted to the inner membrane show mitochondrial  $\text{Ca}^{2+}$  falling faster than that in the cytosol (56). This difference may be a consequence of the highly nonlinear relationship between the steady-state value in the two compartments (Fig. 11) and the fact that the accompanying reduction of  $[\text{NADH}]_m$  that occurs in vivo is not included in the minimal model.

Second, it has been known for some time that  $\text{Ca}^{2+}$  uptake into mitochondria can influence oxidative phosphorylation by decreasing the mitochondrial membrane potential (10). We find in state 3 conditions and at constant levels of  $[\text{NADH}]_m$  that raising the cytosolic  $\text{Ca}^{2+}$  decreases the rate of phosphorylation (Fig. 10C). This effect is quite large at concentrations of  $[\text{Ca}^{2+}]_i$  exceeding 1–2  $\mu\text{M}$  but is significant even at lower, more physiological concentrations. This is due to the depolarizing influence of the increased  $\text{Ca}^{2+}$  current through the uniporter and leads to calculated increases in the rate of oxidation that are comparable to experimental values. Because the rate of  $\text{Ca}^{2+}$  uptake via the uniporter is the key feature of this process, we predict that the influence of  $\text{Ca}^{2+}$  on the rate of ADP phosphorylation will be enhanced by spermine but not by increasing the  $[\text{Na}^+]_i$ .

The stimulation of oxidation and inhibition of phosphorylation by  $\text{Ca}^{2+}$  uptake through the uniporter may have an important regulatory role in insulin secretion by altering the  $[\text{ATP}]:[\text{ADP}]$  ratio. In pancreatic  $\beta$ -cells from *ob/ob* mice cytosolic  $\text{Ca}^{2+}$  has been measured to oscillate out of phase with the ATP-sensitive potassium conductance of the plasma membrane ( $K_{\text{ATP}}$ ) (37). We have previously speculated that  $\text{Ca}^{2+}$  uptake might drive an oscillating conductance by reducing the rate of ATP production when cytosolic  $\text{Ca}^{2+}$  is elevated (28, 40). Although this inhibitory effect by  $\text{Ca}^{2+}$  uptake on ATP production is relatively small, if it occurs at cytosolic  $\text{Ca}^{2+}$  concentrations in which the  $\text{Ca}^{2+}$  stimulation of oxidative phosphorylation via mitochondrial dehydrogenases is maximal, then it could have a major influence on the  $K_{\text{ATP}}$  conductance.

## APPENDIX A

In the original formalism (52), each rate constant of the respiration-driven  $\text{H}^+$  pump diagram (Fig. 2) is a superscripted  $\alpha$  for a unimolecular transition, or an  $\alpha^*$  for a bimolecular one, e.g.,  $\alpha_{12} = \alpha_{12}^*([\text{H}^+]_m)^6$  corresponds to the proton binding of  $1 \rightarrow 2$ . Although redefined to reflect an ideal transfer of 6  $\text{H}^+$  per  $1/2$  NADH oxidized instead of 4  $\text{H}^+$  per  $1/2$  succinate, the unimolecular rate constants used in the  $\beta$ -cell mitochondria model have the same settings as appear in Pietrobon and Caplan (52), with exception of the pair determining the magnitude of the slip cycles, i.e.,  $\alpha_{25} = 6.75 \times 10^{-17}/\text{s}$ ,  $\alpha_{52} = 1.0 \times 10^{-4}/\text{s}$ . Since the concentration of oxidized

product is now a variable,  $\alpha_{43} = \alpha_{43}^*[\text{NAD}^+]_m$ , where the calculated  $\alpha_{43} = 441/\text{s}$  for  $[\text{NADH}]_m/[\text{NAD}^+]_m = 0.04$  is close to the original fixed value of 400/s. For the transition in the opposite direction,  $\alpha_{23} = \alpha_{23}^*[\text{NADH}]_m$  replaces the  $\sqrt{[\text{succinate}]}$  dependence of the Pietrobon-Caplan model, where  $\alpha_{23}^* = 3.405 \times 10^4/(\text{nmol}/\text{mg protein})^{1/2}/\text{s}$ .

## APPENDIX B

The original settings of the  $\alpha_{ij}$  rate constants for the  $\text{F}_1\text{F}_0$ -ATPase-driven  $\text{H}^+$  pump of Fig. 4 (52) have been carried over to the  $\beta$ -cell mitochondria model, with the following exceptions. Since  $[\text{ADP}]_m$  is now a variable,  $\alpha_{43} = \alpha_{43}^*[\text{ADP}]_m$ , where the calculated  $\alpha_{43} = 100/\text{s}$  for  $\alpha_{43}^* = 5.0 \times 10^4/\text{M} \cdot \text{nmol} \cdot \text{mg protein}^{-1} \cdot \text{s}^{-1}$ ,  $[\text{ADP}]_m = 125 \mu\text{M}$  and  $[\text{P}_i]_m = 20 \text{ mM}$  is the same as the original fixed value. For the transition in the opposite direction,  $\alpha_{23}^* = 5.0 \times 10^3/\text{nmol} \cdot \text{mg protein}^{-1} \cdot \text{s}^{-1}$ . The settings  $\alpha_{25} = 1.17 \times 10^{-12}/\text{s}$  and  $\alpha_{52} = 2.0/\text{s}$  for the slip rate constants are typical of a partially uncoupled pump. See Table 3 for parameters.

This work was supported in part by funds from National Science Foundation Grants BIR-9214381 and BIR-9300799, National Institutes of Health Grant R01-RR-10081-01A1, and the Agricultural Experiment Station of University of California, Davis.

Address reprint requests to J. Keizer at the Institute of Theoretical Dynamics.

Received 16 September 1996; accepted in final form 21 April 1997.

## REFERENCES

1. Ashcroft, F., and P. Rorsman. Electrophysiology of the pancreatic  $\beta$ -cell. *Prog. Biophys. Mol. Biol.* 54: 87–143, 1989.
2. Atwater, I., B. Ribalet, and E. Rojas. Cyclic changes in potential and resistance of the  $\beta$ -cell membrane induced by glucose in islets of Langerhans from mouse. *J. Physiol. Lond.* 278: 117–139, 1978.
3. Baysal, K., D. Jung, K. Gunter, T. Gunter, and G. Brierley.  $\text{Na}^+$ -dependent  $\text{Ca}^{2+}$  efflux mechanism of heart mitochondria is not a passive  $\text{Ca}^{2+}/2\text{Na}^+$  exchanger. *Am. J. Physiol. Cell Physiol.* 35: C800–C808, 1994.
4. Berkich, D., G. Williams, P. Masiakos, M. Smith, P. Boyer, and K. LaNoue. Rates of various reactions catalyzed by ATP synthase as related to the mechanism of ATP synthesis. *J. Biol. Chem.* 266: 123–129, 1991.
5. Betina, R., P. Schrier, and E. Slater. Binding of aurovertin to mitochondria and its effect on mitochondrial respiration. *Biochim. Biophys. Acta* 305: 503–518, 1973.
6. Bohnensack, R. The role of the adenine nucleotide translocator in oxidative phosphorylation. A theoretical investigation on the basis of a comprehensive rate law of the translocator. *J. Bioenerg. Biomembr.* 14: 45–61, 1982.
7. Brand, M. The stoichiometry of the exchange catalyzed by the mitochondrial calcium/sodium antiporter. *Biochem. J.* 229: 161–166, 1985.
8. Brand, M., B. Reynafarje, and A. Lehninger. Stoichiometric relationship between energy-dependent proton ejection and electron transport in mitochondria. *Proc. Natl. Acad. Sci. USA* 73: 437–441, 1976.
9. Carafoli, E. The calcium cycle of mitochondria. *FEBS Lett.* 104: 1–15, 1979.
10. Chance, B. The energy-linked reactions of calcium with mitochondria. *J. Biol. Chem.* 240: 2729–2748, 1965.
11. Coll, K., S. Joseph, B. Corkey, and J. Williamson. Determination of the matrix free  $\text{Ca}^{2+}$  concentration and kinetics of  $\text{Ca}^{2+}$  efflux in liver and heart mitochondria. *J. Biol. Chem.* 257: 8696–8704, 1982.
12. Corkey, B., J. Duszyński, T. Rich, B. Matschinsky, and J. Williamson. Regulation of free and bound magnesium in rat hepatocytes and isolated mitochondria. *J. Biol. Chem.* 261: 2567–2574, 1986.



13. **Crompton, M., and I. Heid.** The cycling of calcium, sodium and protons across the inner membrane of cardiac mitochondria. *Eur. J. Biochem.* 91: 599–608, 1978.
14. **Duszyński, J., K. Bogucka, and L. Wojtczak.** Homeostasis of the protonmotive force in phosphorylating mitochondria. *Biochim. Biophys. Acta* 767: 540–547, 1984.
15. **Erecińska, M., and D. Wilson.** Regulation of cellular energy metabolism. *J. Membr. Biol.* 70: 1–14, 1982.
16. **Ghosh, A., P. Ronner, E. Cheong, P. Khalid, and F. Matschinsky.** The role of ATP and free ADP in metabolic coupling during fuel-stimulated insulin release from islet  $\beta$ -cells in the isolated perfused rat pancreas. *J. Biol. Chem.* 266: 22887–22892, 1991.
17. **Gunter, T., K. Gunter, S.-S. Sheu, and C. Gavin.** Mitochondrial calcium transport: physiological and pathological relevance. *Am. J. Physiol.* 267 (Cell Physiol. 36): C313–C339, 1994.
18. **Gunter, T., and D. Pfeiffer.** Mechanisms by which mitochondria transport calcium. *Am. J. Physiol.* 258 (Cell Physiol. 27): C755–C786, 1990.
19. **Hafner, R., G. Brown, and M. Brand.** Thyroid-hormone control of state-3 respiration in isolated rat liver mitochondria. *Biochem. J.* 265: 731–734, 1990.
20. **Hajnóczky, G., L. Robb-Gaspers, M. Seitz, and A. Thomas.** Decoding of cytosolic calcium oscillations in the mitochondria. *Cell* 82: 415–424, 1995.
21. **Hehl, S., A. Golard, and B. Hille.** Involvement of mitochondria in intracellular calcium sequestration by rat gonadotrophs. *Cell Calcium* 20: 515–524, 1996.
22. **Hill, T.** *Free Energy Transduction in Biology.* New York: Academic, 1977, p. 1–102.
23. **Hougaard, D., J. Nielsen, and L.-I. Larsson.** Localization and biosynthesis of polyamines in insulin-producing cells. *Biochem. J.* 238: 43–47, 1986.
24. **Jensen, B., K. Gunter, and T. Gunter.** The efficiencies of the component steps of oxidative phosphorylation. II. Experimental determination of the efficiencies in mitochondria and examination of the equivalence of membrane potential and pH gradient in phosphorylation. *Arch. Biochem. Biophys.* 248: 305–323, 1986.
25. **Johnston, J., and M. Brand.** Stimulation of the respiration rate of rat liver mitochondria by sub-micromolar concentrations of extramitochondrial  $\text{Ca}^{2+}$ . *Biochem. J.* 245: 217–222, 1987.
26. **Joseph, S., K. Coll, R. Cooper, J. Marks, and J. Williamson.** Mechanisms underlying calcium homeostasis in isolated hepatocytes. *J. Biol. Chem.* 258: 731–741, 1983.
27. **Keizer, J.** *Statistical Thermodynamics of Nonequilibrium Processes.* New York: Springer-Verlag, 1987, chapt. 5, p. 177–234.
28. **Keizer, J., and G. Magnus.** The ATP-sensitive potassium channel and bursting in the pancreatic beta cell. A theoretical study. *Biophys. J.* 56: 229–242, 1989.
29. **Klingenberg, M.** The ADP-ATP carrier in mitochondrial membranes. In: *The Enzymes of Biological Membranes*, edited by A. Martonosi. New York: Plenum, 1976, vol. 3, p. 383–438.
30. **Klingenberg, M., and H. Rottenberg.** Relation between the gradient of the ATP/ADP ratio and the membrane potential across the mitochondrial membrane. *Eur. J. Biochem.* 73: 125–130, 1977.
31. **Kramer, R., and M. Klingenberg.** Modulation of the reconstituted adenine nucleotide exchange by membrane potential. *Biochemistry* 19: 556–560, 1980.
32. **Krishnamoorthy, G., and P. Hinkle.** Non-ohmic proton conductance of mitochondria and liposomes. *Biochemistry* 23: 1640–1645, 1984.
33. **Kröner, H.**  $\text{Ca}^{2+}$  ions, an allosteric activator of calcium uptake in rat liver mitochondria. *Arch. Biochem. Biophys.* 251: 525–535, 1986.
34. **Kröner, H.** The real kinetics of the mitochondrial calcium uniporter of the liver and its role in cell calcium regulation. *Biol. Chem. Hoppe Seyler* 369: 149–155, 1987.
35. **Kröner, H.** Spermine, another specific allosteric activator of calcium uptake in rat liver mitochondria. *Arch. Biochem. Biophys.* 267: 205–210, 1988.
36. **LaNoue, K., and A. Schoolwerth.** Metabolite transport in mitochondria. *Ann. Rev. Biochem.* 48: 871–922, 1979.
37. **Larsson, O., H. Kindmark, R. Bränström, B. Fredholm, and P.-O. Berggren.** Oscillations in  $\text{K}_{\text{ATP}}$  channel activity promote oscillation in cytoplasmic free  $\text{Ca}^{2+}$  concentration in the pancreatic  $\beta$  cell. *Proc. Natl. Acad. Sci. USA* 93: 5161–5165, 1996.
38. **Lehninger, A.** *Biochemistry* (2nd ed.). New York: Worth, 1977, p. 515.
39. **Ligeti, E., and A. Fonyó.** Reactivity of the sulphhydryl groups of the mitochondrial phosphate carrier. *Eur. J. Biochem.* 167: 167–173, 1984.
40. **Magnus, G.** *A Mitochondria-Based Model for Bursting and its D-Glucose Dependence in the Pancreatic Beta Cell* (PhD thesis). Davis, CA: University of California, 1995.
41. **Malaisse, W., and A. Sener.** Glucose-induced changes in cytosolic ATP content in pancreatic islets. *Biochim. Biophys. Acta* 927: 190–195, 1987.
42. **McCormack, J.** Effects of spermine on mitochondrial  $\text{Ca}^{2+}$  transport and the ranges of extramitochondrial  $\text{Ca}^{2+}$  to which the matrix  $\text{Ca}^{2+}$ -sensitive dehydrogenases respond. *Biochem. J.* 264: 167–174, 1989.
43. **McCormack, J., H. Browne, and N. Dawes.** Studies on mitochondrial  $\text{Ca}^{2+}$ -transport and matrix  $\text{Ca}^{2+}$  using fura-2-loaded rat heart mitochondria. *Biochim. Biophys. Acta* 973: 420–427, 1989.
44. **McCormack, J., A. Halestrap, and R. Denton.** Role of calcium ions in regulation of mammalian intramitochondrial metabolism. *Physiol. Rev.* 70: 391–425, 1990.
45. **McCormack, J., E. Longo, and B. Corkey.** Glucose-induced activation of pyruvate dehydrogenase in isolated rat pancreatic islets. *Biochem. J.* 267: 527–530, 1990.
46. **Meglasson, M., and F. Matschinsky.** Pancreatic islet glucose metabolism and regulation of insulin secretion. *Diabetes Metab. Rev.* 2: 163–214, 1986.
47. **Mitchell, P.** Chemiosmotic coupling and energy transduction. In: *Theoretical and Experimental Biophysics. A Series of Advances*, edited by A. Cole. New York: Dekker, 1969, vol. 2, p. 159–216.
48. **Monod, J., J. Wyman, and J. Changeux.** On the nature of allosteric transitions: a plausible model. *J. Mol. Biol.* 12: 88–102, 1965.
49. **Moreno-Sánchez, R.** Regulation of oxidative phosphorylation in mitochondria by external free  $\text{Ca}^{2+}$  concentrations. *J. Biol. Chem.* 260: 4028–4034, 1985.
50. **Pace, C. S., J. T. Tarvin, and J. S. Smith.** Stimulus-secretion coupling in  $\beta$ -cells: modulation by pH. *Am. J. Physiol.* 244 (Endocrinol. Metab. 7): E3–E18, 1983.
51. **Pietrobon, D., G. Azzone, and D. Walz.** Effect of fusiculin and antimycin A on the redox-driven  $\text{H}^+$ -pumps in mitochondria: on the nature of “leaks.” *Eur. J. Biochem.* 117: 389–394, 1981.
52. **Pietrobon, D., and S. Caplan.** Flow-force relationships for a six-state proton pump model: intrinsic uncoupling, kinetic equivalence of input and output forces, and domain of approximate linearity. *Biochemistry* 24: 5764–5778, 1985.
53. **Pietrobon, D., M. Zoratti, G. Azzone, and S. Caplan.** Intrinsic uncoupling of mitochondrial proton pumps. 2. Modeling studies. *Biochemistry* 25: 767–775, 1986.
54. **Pietrobon, D., M. Zoratti, G. Azzone, J. Stucki, and D. Walz.** Non-equilibrium thermodynamic assessment of redox-driven  $\text{H}^+$  pumps in mitochondria. *Eur. J. Biochem.* 127: 483–494, 1982.
55. **Rizzuto, R., P. Bernardi, M. Favaron, and G. Azzone.** Pathways for  $\text{Ca}^{2+}$  efflux in heart and liver mitochondria. *Biochem. J.* 246: 271–277, 1987.
56. **Rizzuto, R., A. Simpson, M. Brini, and T. Pozzan.** Rapid changes of mitochondrial  $\text{Ca}^{2+}$  revealed by specifically targeted recombinant aequorin. *Nature Lond.* 358: 325–327, 1992.
57. **Rutter, G., J.-M. Theler, M. Murgia, C. Wollheim, T. Pozzan, and R. Rizzuto.** Stimulated  $\text{Ca}^{2+}$  influx raises mitochondrial free  $\text{Ca}^{2+}$  to supramicromolar levels in a pancreatic  $\beta$ -cell line. Possible role in glucose and agonist-induced insulin secretion. *J. Biol. Chem.* 268: 22385–22390, 1993.
58. **Saavedra-Molina, A.** Control of mitochondrial matrix calcium: studies using fluo-3 as a fluorescent calcium indicator. *Biochem. Biophys. Res. Commun.* 167: 148–153, 1990.
59. **Scarpa, A., and A. Azzi.** Cation binding to submitochondrial particles. *Biochim. Biophys. Acta* 150: 473–481, 1968.
60. **Somlyo, A., M. Bond, and A. Somlyo.** Calcium content of mitochondria and endoplasmic reticulum in liver frozen rapidly in vivo. *Nature Lond.* 314: 622–625, 1985.



61. **Sparagna, G., K. Gunter, S.-S. Sheu, and T. Gunter.** Mitochondrial calcium uptake from physiological-type pulses of calcium. A description of the rapid uptake mode. *J. Biol. Chem.* 260: 27510–27515, 1995.
62. **Tischler, M., P. Hecht, and J. Williamson.** Determination of mitochondrial/cytosolic metabolite gradients in isolated rat liver cells by cell disruption. *Arch. Biochem. Biophys.* 181: 278–292, 1977.
63. **Tzagoloff, A.** *Mitochondria*. New York: Plenum, 1982, p. 62–180.
64. **Unger, R.** Diabetic hyperglycemia: Link to impaired glucose transport in pancreatic beta cells. *Science Wash. DC* 251: 1200–1205, 1991.
65. **Wilson, D., D. Nelson, and M. Erecińska.** Binding of the intramitochondrial ADP and its relationship to adenine nucleotide translocation. *FEBS Lett.* 143: 228–232, 1982.
66. **Wingrove, D., J. Amatruda, and T. Gunter.** Glucagon effects on the membrane potential and calcium uptake rate of rat liver mitochondria. *J. Biol. Chem.* 259: 9390–9394, 1984.
67. **Wingrove, D., and T. Gunter.** Kinetics of mitochondrial calcium transport. II. A kinetic description of the sodium-dependent calcium efflux mechanism of liver mitochondria and inhibition by ruthenium red and by tetraphenylphosphonium. *J. Biol. Chem.* 261: 15166–15171, 1986.
68. **Yousufzai, S., M. Bradford, E. Shrago, and R. Ewart.** Characterization of the adenine nucleotide translocase of pancreatic islet mitochondria. *FEBS Lett.* 137: 205–208, 1982.
69. **Zoratti, M., M. Favaron, D. Pietrobon, and G. Azzone.** Intrinsic uncoupling of mitochondrial proton pumps. 1. Non-ohmic conductance cannot account for the nonlinear dependence of static head respiration on  $\Delta\tilde{\mu}_{\text{H}}$ . *Biochemistry* 25: 760–767, 1986.

